UTILIZING MICRO COMPUTED TOMOGRAPHY DATA TO PRODUCE IMPLANTABLE SCAFFOLDS FOR ORTHOPEDIC TISSUE ENGINEERING

by

BRANDI CHARMAINE TELLIS

A Thesis Submitted to the Faculty of the

BIOMEDICAL ENGINEERING PROGRAM

in Partial Fulfillment of the Requirements For the Degree of

MASTER OF SCIENCE

In the Graduate College of

THE UNIVERSITY OF ARIZONA

2006

STATEMENT BY AUTHOR

This thesis has been submitted in partial fulfillment of requirements for an advanced degree at the University of Arizona and is deposited in the University Library to be made available to borrowers under rules of the Library.

Brief quotations from this thesis are allowable without special permission, provided that accurate acknowledgement of the source is made. Requests for permission for extended quotation from or reproduction of this manuscript in whole or in part may be granted by the head of the major department or the Dean of the Graduate College when in his or her judgment the proposed use of the material is in the interests of scholarship. In all other instances, however, permission must be obtained from the author.

SIGNED: 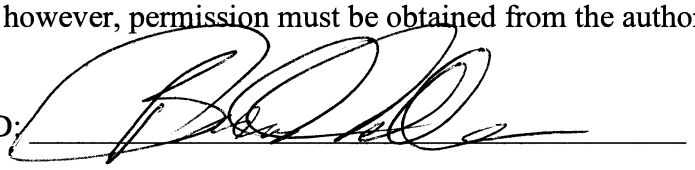

APPROVAL BY THESIS DIRECTOR

This thesis has been approved on the date shown below:

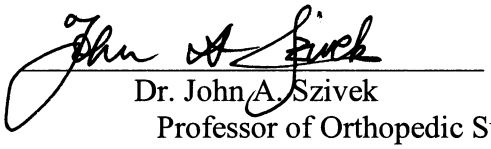

Dr. John A. Szivek

Oct 9/2006

Date

Professor of Orthopedic Surgery and Biomedical Engineering.

Acknowledgments

My thesis committee:

John A. Szivek, Ph.D

Jonathan Vande Geest, Ph.D

Ted Trouard, Ph.D

I'd like to thank my thesis committee for all of their advice, diligence, and, most of all, for their patience.

I'd also like to acknowledge the financial support of the National Institutes of Health, through the National Institute of Biomedical Imaging and Bioengineering (Grant # R01EB00661).

I thank Advanced Ceramics Research of Tucson, Arizona, for the use of their equipment and for the support, help and advice from:

Ranji Vaidyanathan, Ph.D,
Greg Artz,
Tom Phillips,
Kurt Knittel,
and
Christina Bisch

Last, but not least, I must thank my fellow students and friends in the Orthopedics Research Laboratory for making an educational experience a fun one as well:

Cody Bliss,
David Margolis,
Chris Geffre,
and
Andrew Schnepp

This work is dedicated to my mother,
Priscilla Tellis
The best mother anyone could ever want.

In loving memory of
Charles Tellis,
Mary Gilmore Tellis-Vallion,
and
Richard Simon Vallion

TABLE OF CONTENTS

TABLE OF CONTENTS – CONTINUED

LIST OF ILLUSTRATIONS

LIST OF TABLES

Abstract

Tissue engineering requires a three dimensional porous matrix that provides mechanical support and a template for new tissue growth, as well as allowing vascularization for nutrient delivery and waste product removal. Multiple methods exist for producing porous tissue engineering scaffolds from biocompatible materials. The combination of high resolution imaging systems and rapid prototyping techniques, however, has opened the door to producing scaffolds whose pore structures can match that of the tissue being repaired.

A micro computed tomography scanner was used to scan trabecular bone samples from adult male canines, producing three dimensional bone models. These data sets were exported to a computer aided drawing program, where further customization of the data was performed. Additional features were added to the trabecular bone-like pore structure to allow the attachment of strain gauges to the scaffold, as well as achieve an anatomical fit with the intended surgical implant site. The customized scaffolds, made of polybutylene terephthalate (PBT), were produced using a fused deposition modeler. Morphological analysis, mechanical testing and degradation studies were performed to compare the trabecular-like scaffolds, to those with conventionally-designed pore structures.

Morphological analysis revealed that the trabecular-like scaffolds matched the bone samples from which they were made in porosity only, requiring an improvement in modeler resolution to better match bone properties such as connectivity density and trabecular number. Mechanical testing showed that the trabecular-like scaffolds and simple pore structured scaffolds possessed a compressive stiffness within the range reported for human trabecular bone, with the trabecular-like scaffolds having a greater compressive stiffness than the complex pore structured scaffolds originally produced to duplicate trabecular bone. Degradation studies show that the mechanical properties and morphology of porous scaffolds made of PBT remained constant after three months soaking in a 37°C saline solution.

1 Introduction

According to the Arthritis Foundation, over twenty million Americans suffer pain and disability from cartilage injuries (1). Additionally, over 250,000 allogenic bone transplant operations are performed yearly to repair segmental bone defects arising from trauma and the removal of bone tumors (2). The poor natural healing response of cartilage injuries has led to the development of a number of approaches that attempt to repair cartilage defects. These techniques include soft tissue grafts, marrow stimulation, osteochondral transfer (Mosaicplasty®), as well as autologous chondrocyte implantation (ACI), which is a cell transplantation technique.

Recently, cartilage tissue engineering on porous three-dimensional scaffolds has shown promise as a potential technique for cartilage defect repair (3). Scaffolds can provide a reproducible, biocompatible, and biodegradable structure capable of mimicking the mechanical characteristics of bone while supporting cells and delivering bioactive molecules (4-6). Depending on the scaffold material and manufacturing technique, it is possible to develop scaffolds having one section upon which cartilage can be grown in vitro, and another section possessing a pore structure that closely resembles that of trabecular bone. This thesis focuses on the production of scaffolds designed to facilitate bone in-growth which have a biomimetic pore structure.

Useful scaffold properties include an interconnected pore network that allows cell growth, transport of nutrients and waste, and controllable degradation and resorption rates that may potentially match tissue replacement rates (7, 8). A suitable surface chemistry (9-11) and microstructure (12-14) is necessary for cell attachment, proliferation, and differentiation (15-17). In addition, the mechanical properties of the

scaffold should be sufficient to protect new tissue from excessive loading (5, 6, 18), including wound contraction forces (19).

Scaffolds with interconnected pores have been produced by a variety of fabrication techniques such as solvent casting/particulate leaching (20-22), fiber bonding, (23-25) and thermally induced phase separation (TIPS) (26, 27). However, concerns over incomplete evaporation of toxic organic solvents, limited reproducibility, and long preparation times using these techniques (28) have spurred interest in alternative methods. Free form fabrication (FFF) is a solvent-free technique capable of creating highly reproducible scaffold structures whose interconnected pores may vary in size and orientation across the matrix. This technique is useful for engineering scaffolds to be used at the interface between two or more tissues (18, 29). As such it can be useful for applications in which both bone and cartilage require repair. Free form fabrication techniques include stereolithography (SLA) (30-32), selective laser sintering (SLS) (30-33), 3D printing (3DP) (30-34), and fused deposition modeling (FDM) (5, 30-32).

The SLA process, which consists of scanning a UV laser beam over a bath of photopolymerizable liquid polymer to build a 3D object, is currently used for the production of anatomical models for surgical planning (35). Until recently, extensive post processing and a lack of photopolymerizable, biocompatible/biodegradable polymers with the proper mechanical properties, have limited the use of SLA for scaffolds (36). With the recent development of photocurable biodegradable copolymers such as poly-ε-caprolactone-*co*-trimethylene carbonate (37) and μSLA devices with micrometer resolution (38), SLA has been used in a broader range of applications. Stereolithography still has its drawbacks, including the required post-processing of "green" parts by curing

in an ultraviolet light chamber, the possible formation of cavities in the part that may trap liquid resin, and the occasional need of a solvent to cleanse insufficiently drained resin from the surface (31).

SLS uses a CO_2 laser directed at a polymer or ceramic particles to raise the temperature of the powder to just above the material's glass transition temperature, fusing the particles into a solid mass (31, 32). SLS appears to be useful primarily for the preparation of scaffolds to be used in bone and it has been used to manufacture calcium phosphate ceramic bone implants from particles (39). These scaffolds were biocompatible and osteoconductive in a canine model (40). Disadvantages of SLS include a process more mechanically complex than most other FFF techniques, finished parts having an absorbent, powdery surface that may complicate sterilization, and the pore structure may vary across the body of the finished part due to variations in particle size (31).

In 3DP, an inkjet print head sprays a binding agent over a layer of powder, after which a fresh layer of powder is rolled over the first, merging the two layers (31, 33). The process is repeated until the entire object is built, which must be fully dried before being removed from the loose powder. Although the 3DP process takes place at ambient temperature, there are several drawbacks, including a significant processing time to convert biocompatible polymers to a suitable powder, and difficulty in removing loose powder from within a porous construct (29).

Like the other free-form fabrication techniques, the fused deposition modeling (FDM) process utilizes 3D objects produced in a CAD program or from data sets created by imaging systems, to produce highly reproducible interconnected porous scaffolds. A

thermoplastic polymer is heated to a semi-liquid state and extruded through a fine extrusion tip a few thousandths of an inch in diameter. The fine extruded filament is called a raster. The extrusion head assembly is guided as it moves in the X-Y plane by software that divides the 3D object into 2D slices (41). Moving either the extrusion head or the stage and repeating the process builds the remaining layers. Pore structures are determined by the values entered into the control software for parameters such as raster thickness, raster gap width (space between rasters), and raster angle (42), while layer thickness is largely determined by the extrusion tip diameter (31). Although "man-made" pores can be designed by adjusting software values, imaging techniques such as micro computed tomography (μCT) can be utilized to produce a data set which can be used to build a scaffold whose pore morphology mimics bone (43). This is useful because the micro architecture of a scaffold is believed to be vital to the coordination of cellular processes, along with the simulation of appropriate mechanical properties, and the integration of the scaffold with surrounding tissues and microcirculation (4). Using a CAD program, it is possible to create scaffolds produced from 3D data sets with combinations of micro CT imaged data and geometric patterns. The inclusion of features, such as domes to fit the curvature of a tissue surface and cylindrical rings and struts designed to add stability and strength to the scaffold's "trabeculated" structure, are also possible.

Imaging techniques such as CT have been used for preoperative planning and for adding features to customized implants to aid surgeons and to improve patient outcomes (44-47). However, there have been few studies focusing on the microstructure of biomedical implants.

In addition to improved integration at the defect-implant interface, high resolution imaging, CAD, and rapid prototyping can be used to add additional functionality to medical implants. One example is the addition of strain gauges to orthopedic implants (48, 49), which enables in vivo strain measurement. This can lead to a better understanding of the effect of in vivo loading on regenerating tissue, and eventually provide physicians with a new means of evaluating patient healing.

It was the goal of this study to develop and create polymeric scaffolds via FDM based on data obtained from a μCT scan of canine trabecular bone. The mechanical stiffness of the "trabeculated" scaffold was compared to that of simple and complex porous scaffolds whose structure was created with a CAD program. Morphological properties such as porosity, connectivity density, and trabecular spacing of each scaffold type and canine trabecular bone were also compared utilizing μCT analysis software. Following this, μCT scan data obtained from scanning canine trabecular bone was used as the basis for customized implants whose additional features, such placement sites for strain gauges, were added using a commercially available CAD package. These scaffolds were produced via FDM, and evaluated for degradation under simulated physiologic conditions to measure changes in scaffold structure, ultimate compressive stress, and apparent modulus over a period of three months.

2 Materials and Methods:

2.1 Experiment I: Creation of Trabecular Scaffolds

2.1.1 Micro Computed Tomography

Two samples were collected from the bones of an adult male hound obtained by the University of Arizona's Animal Care Facility in keeping with the approved Institutional Animal Care and Use Committee (IACUC) protocol #05-003. One was 12mm in diameter and 4.5mm long and was taken from the medial femoral chondyle and one 19.1mm in diameter and 25.4mm long from the femoral head. The bone samples were placed into the sample holder of a desktop fan-beam micro CT scanner (μCT-20, Scanco Medical AG, Switzerland) and scanned at medium resolution (600 x-ray projections with 512 X 512 pixels bitmap image, 18 μm resolution). Integration time was set to 200 ms. Four hundred eighty-nine slices of the femoral head sample and 150 slices of the medial condyle sample were scanned, with each slice representing 30 μm-thick segments of the sample. Once the scans were complete, 2D slices of each sample were viewed. The larger specimen collected from the femoral head was manufactured into a scaffold. To segment the slices into a 3D model, a volume of interest (VOI) was selected in the "Evaluation" program of the scanner's software. A circle (5.6 mm diameter) was drawn onto a section of the image of the bone in the central region of the sample. Using the Morph function, the circle was copied over a range of 112 slices creating a 3D cylinder approximately 3.4 mm in length and 5.6 mm in diameter. A 3D segmentation of the VOI was done with a Sigma-Gauss value of 1.2, a support value of 2, and a threshold value of 200. The Sigma-Gauss and Support parameters "smear" the binary values of a 3D image file from "black and white" to "shades of gray," producing smoother surfaces. The threshold value sets the pixel brightness of pixels in each image slice that will be

selected to comprise the 3D model. Once segmentation was complete, a 3D image of the bone was created and saved into a seg.aim file, which is a proprietary Scanco 3D image file format.

Scanco's image processing language (IPL) commands were used to first read the seg.aim file into memory and then convert it to an ASCII stereolithography (STL) file and export it via FTP in order to build the scaffold in the fused deposition modeler. Multiple sections of the femoral head sample were later segmented to obtain a range of values for the morphometric properties porosity, connectivity density, and trabecular separation for comparison to those of the manufactured trabecular scaffolds.

2.1.2 Building the "Trabecular" Scaffold

Unfilled polybutylene terephthalate (Valox 315, GE Plastics, North America) pellets were melted at 250^{o}C and formed into a 1.70 mm diameter filament using a Haake single-screw polymer extruder (Thermo Electron Corporation) and loaded into the FDM. A commercially available support filament (P-400 Release, Stratasys, Inc., Eden Prairie MN, USA) was also loaded.

The trabecular .stl file was opened in QuickSlice, the STL-processing software accompanying the rapid prototyper (FDM 1600, Stratasys, Inc., Eden Prairie MN, USA). The FDM 1600 has a tolerance of ± 0.005 inches for parts less than 5 inches in diameter when using a manufacturer-provided polymer filament. The STL file was scaled up by a factor of 2.54 before being converted to slices to improve modeler resolution. After the 3D trabecular model was divided into slices, a support base (created by deposition of the P-400 Release) was added to create a barrier between the trabecular scaffold and the

foam stage within the modeler. The extrusion road paths were then set using the road width 0.51 mm for the rasters and the perimeter, and the raster gap width and perimeter-and-roads gap width set to -0.0030 inches (0.076 mm) so that the rasters would overlap each other by 0.076 mm. The raster angles, or the angles at which the PBT are laid down onto each sucessive layer, were set to 0 and 90 degrees. The words raster and perimeter refer to the fine filament of melted polymer whose diameter is defined by the diameter of the extrusion tip (0.010 inches) and the rate of extrusion. The perimeter is the filament that is laid down along the outer edge of each slice of the object being built, while the raster is the linear filament, several of which are laid down to fill in the area of each slice. The file was exported as a Stratasys Machine Language (SML) file for upload into the FDM. The extrusion temperatures used for the model material and support material were 255^{O}C and 265^{O}C, respectively. The extrusion temperature used for the support material was recommended by the manufacturer, while the 255^{O}C PBT extrusion temperature was arrived at after a trial and error process of visual inspection of scaffolds produced at different PBT temperatures. After the scaffold was built, the support layer was peeled away. A photograph of the FDM creating a scaffold is shown in Figure 1. Eighteen trabecular scaffolds were created and this group was labeled 2p54trab (Figure 2B).

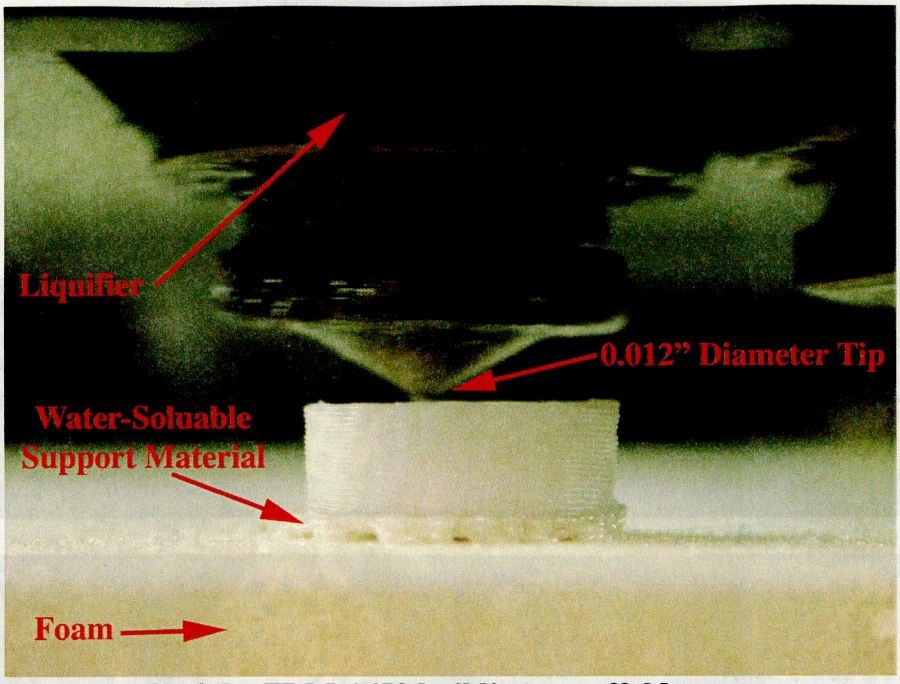

Figure 1: Photograph of the FDM-1650 building a scaffold

2.1.3 Design and Manufacturing of the Simple Linear Pore and Complex Interconnected Pore Scaffolds

QuickSlice was used to create a series of slices of a cylinder 13.5 mm in diameter and 10 mm in height. Four scaffold types were created by setting different values for the raster gap width, road width, and raster angles as shown in Table 1. The simple linear pore scaffold groups, containing 18 scaffolds each, had cube-shaped pores formed by orthogonal rasters (Figure 2B and 2C). The complex interconnected pore groups, containing 18 scaffolds each, had a honeycomb-like pore structure (Figure 2D and 2E) achieved by giving alternating sets of two sequential slices raster angle values of 0^{o}, 90^{o} and 45^{o}, -45^{o} respectively (Table 1).

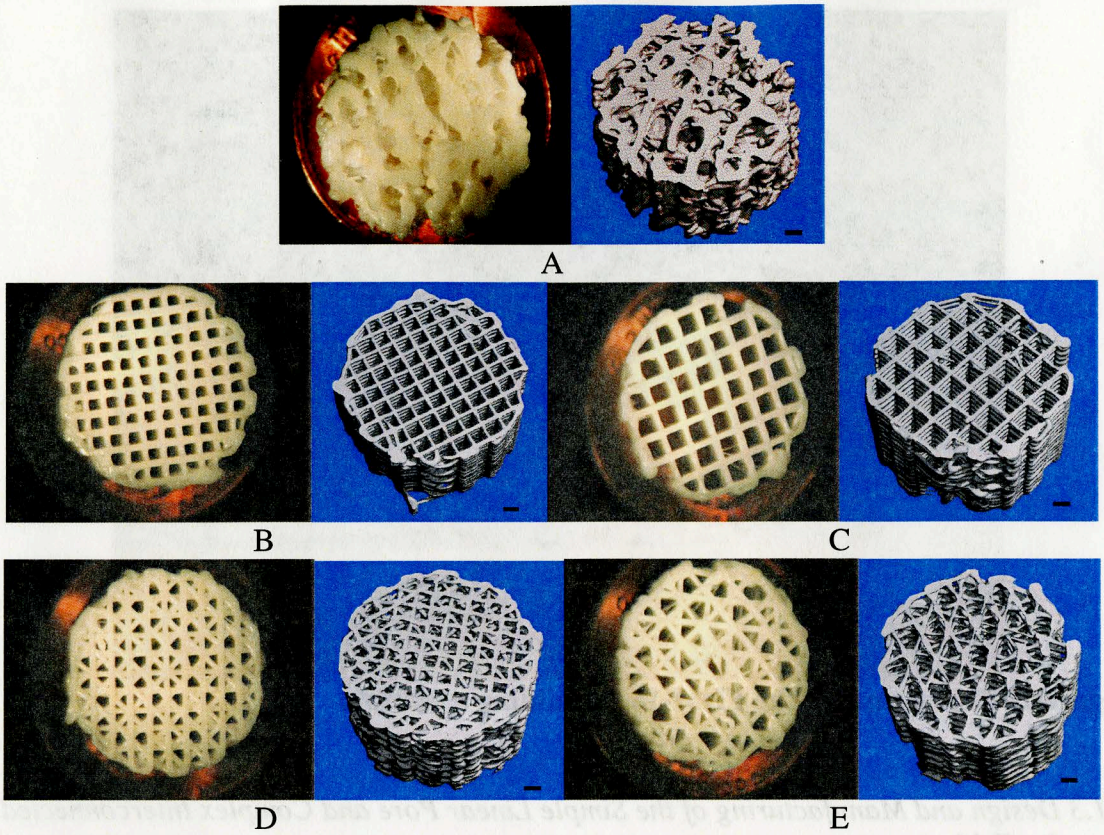

Figure 2: Digital photographs and micro CT 3D segmentations of polybutylene terephthalate scaffolds. The scaffolds are photographed on top of a penny for reference. Scale bars in 3D segmentations represent 1 mm. A: 2p54trab, B: 90deg30, C: 90deg50, D: 9045deg30, and E: 9045deg50

Table 1: Quickslice Parameters for the designed Simple Linear Pore and Complex Interconnected Pore scaffold groups. "Small" and "large" refer to the relative pore sizes of each design.

Scaffold group	Scaffold Type	Raster gap width	Road width	Raster angles
90deg30	Simple small	0.76 mm (0.030")	0.51 mm	0^o, 90^o
90deg50	Simple large	1.27 mm (0.050")	0.51 mm	0^o, 90^o
9045deg30	Complex small	0.76 mm (0.030")	0.51 mm	0^o, 90^o, 45^o, -45^o
9045deg50	Complex large	1.27 mm (0.050")	0.51 mm	0^o, 90^o, 45^o, -45^o

2.1.4 Preparation for mechanical testing

All 90 scaffolds (18 scaffolds in each of the five groups) were surface ground with a GP-25 Grinder Polisher (LECO Corp., St. Joesph, MI USA) using a very fine 1200 grit carbide paper (LECO Corp., St. Joesph, MI USA) to produce smooth, flat surfaces for compression testing. A bull's eye circular level was used to assess planeness.

Following grinding, the height and diameter of each scaffold was measured using a vernier caliper (Kanon, Japan).

2.1.5 Mechanical Testing

Eighteen scaffolds of each type were divided into three subgroups (n = 6). One subgroup of scaffolds was tested in compression first at 49 N/s and then at 294 N/s. These two load rates were chosen to represent loading at a walking gait and while running. Loads were selected to establish stiffness and prevent damage to the scaffold and therefore allow post-compression morphological analysis. The compression tests were carried out on a servo hydraulic test machine (MTS) in load control. Peak loads of either 5 kg (49 N), or 30 kg (294 N) were applied within one second. The scaffolds were not pre-conditioned or pre-loaded. The second subgroup of scaffolds were soaked in 0.09% NaCl solution at 25°C for seven days and tested in compression at 49 N/s. The third subgroup of scaffolds were soaked in 0.09% NaCl solution at 25°C for seven days and tested in compression at 294 N/s.

Scaffolds were compressed axially on a mechanical test system (Model 810, MTS, Minneapolis, MN, USA) to assess stiffness. For each compression cycle, load (kgf) and stroke (mm) were collected simultaneously with data collection software (LabView 5.0.1, National Instruments, Austin, TX) through a Ni-DAQ data acquisition board into a Macintosh G4 computer and saved into a spreadsheet.

Load and stroke from each test run on a scaffold were used for calculation of the compressive modulus of each group of scaffolds. Maximum load, minimum load, maximum stroke, and minimum stroke of each test run on a scaffold were used for

calculation of the apparent compressive modulus of each group of scaffolds. To establish stresses on the scaffolds, the following formula was used:

$\sigma = ((L/A)/1 \text{ X } 10^6)$; where
L = difference between maximum and minimum load, in N
A = measured contact area of the scaffold, in m^2
σ = Stress, in MPa

To get a strain value (in %), the following formula was used:
$\varepsilon = 1-((H-S)/H)*100)$; where
H = measured height of the scaffold, in m
S = difference between maximum and minimum stroke values, in m
ε = strain, in %

The apparent compressive modulus, in MPa, was calculated using:
modulus = σ/ε.

2.1.6 Morphological analysis using Micro CT

Four scaffolds from each of the five groups were placed into the sample holder of the μCT and scanned at standard resolution (250 x-ray projections, 512 X 512 pixel bitmap images, with resolution of 18 μm), with an integration time of 160 ms.

On the scanned image of the scaffold, an outline was drawn around the outer edge of the scaffold with the free-hand drawing tool. This outline was copied onto successive slices until a VOI was created encompassing the entire scaffold. A Sigma-Gauss of 1.2, a support of 2, and a threshold of 50 were used for segmentation. Porosity, connectivity density, and trabecular spacing were determined and averaged. Porosity is defined as the ratio of the volume of open space to the total volume of the sample. Connectivity density is the maximum number of trabecular connections that must be broken in order to break a trabecular sample into two parts (50). Trabecular spacing, or separation, is the average distance between trabecular struts.

2.1.7 Statistical Analysis

In all tests, an ANOVA was performed to determine whether a significant difference between the scaffold groups was present. A Tukey HSD post hoc test was then used to determine where the differences lay, with a p-value ≤ 0.05 being statistically significant.

2.2 Experiment II: Creation of Inverse Trabecular Scaffolds

The sample collected from the femoral head of the femur of a test animal that was used to produce trabecular-like scaffolds in Experiment I was also imaged to create a 3D data set that was the basis of a series of customized trabecular scaffolds used in this series of experiments. The same micro computed tomography scanner (μCT-20, Scanco Medical AG, Switzerland) was used to image the bone for these experiments.

2.2.1 Modification of CT Scan Data

The original 3D model of the trabecular bone sample underwent extensive modification to customize the scaffold for implantation into the next group of test animals used in a sensate scaffold study. To accommodate sensors, attachment sites were added to the scaffold design, which enabled strain gauge attachment (Figure 3).

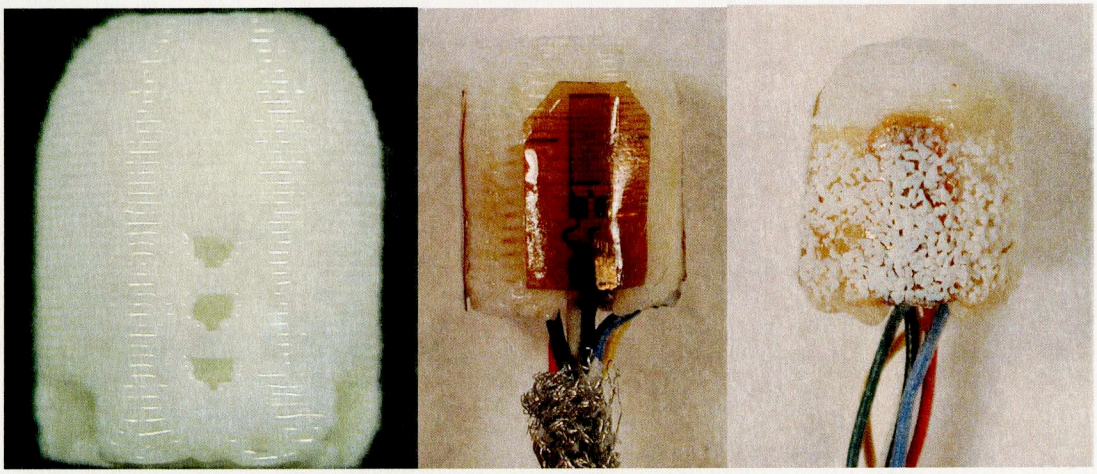

A B C

Figure 3: Complex Pore scaffold. A: Complex Pore scaffold as produced by the Stratasys RP-1650. B: Scaffold shown with strain gauges attached. C: Strain-gauged scaffold as prepared for implantation, being coated with CPC particles.

This facilitated easy placement of the "sensate" scaffolds and allowed load measurement in the knee joints of dogs during various activities. In addition, the scaffold was designed with a rounded joint interfacing surface, which would serve as an artificial subchondral

layer, on which tissue engineered cartilage could ultimately be grown. The curvature of this surface was prepared to match the shape of the medial chondyle of a dog. When implanted, the top of the scaffold was designed to sit one millimeter below the cartilage surface. The scaffold was designed to be recessed into the medial chondyle because a goal of the program that this study was a part of was to grow a functional cartilage layer onto the surface of the scaffold before implantation into a joint.

The rapid prototyping modeler (FDM-1650, StrataSys, Eden Prairie MN, USA) was used to manufacture the scaffolds that were used in these experiments. It was necessary to scale up the 3D model of the scaffold by a factor of 2.5X, in order to build scaffolds with an acceptable pore structure because the modeler used to manufacture the scaffolds was originally designed for building larger objects (up to 16 cm^3). To create a customized scaffold with the required dimensions, the "Evaluation" program in the CT scanner's software was used to create a volume of interest (VOI). This was done by drawing a circle (3.5 mm in diameter) onto a section of a slice image of the bone in the central region of the sample. Using the "Morph" function, the circle was copied onto a range of 124 slices. These 124 slices were stacked onto each other during the "Segmentation" step of the process, creating a 3D bone model cylinder approximately 3.72 mm in length and 3.56 mm in diameter. The 3D model was saved in the Scanco proprietary seg.aim file format. Once scaled up by 2.5 times, the cylinder size would be 9.3 mm in length and 8.9 mm in diameter, leaving room for further modification using a computer aided drawing (CAD) program.

2.2.2 Creating an Inverse Pore Structure

The next modification to the 3D model of trabecular bone produced from the micro CT scan was to create an inverse, "inside out" trabecular pore structure. This was done to provide a template for bone growth that would enable the new bone growing through the scaffold to better resemble natural trabecular bone. As described in Experiment I, Scanco's image processing language (IPL) commands were used to first read the 3D seg.aim file into memory, then the 3D model was turned "inside out" using the "set_value" and "gobj" commands. Unfortunately, this left an inverse trabecular structure whose pores were too small to be useful. The "peel3dout" command was used to "peel" away voxels (the smallest unit of a 3D image) until the structure was deemed to be porous enough while still maintaining adequate structural integrity. The degree to which the voxels are "peeled" away was determined by the peel factor value used with the "peel3dout" command.

Through a trial and error process of visual inspection of each 3D model, a peel factor of 3 was determined to provide the optimum porosity while maintaining structural integrity, meaning that the structure was not too fragile to be press-fit into a surgical defect site. The finished 3D inverse trabecular model was then saved as a new seg.aim file. This new seg.aim file was converted to an American Standard Code for Information Interchange (ASCII) stereolithography (STL) file and exported for further modification with a CAD program.

2.2.3 Using CAD to Add Customized Features

The "peeled" 3D inverse trabecular STL file was opened in SolidWorks (SolidWorks Student Edition 2003-2004, SolidWorks Corporation, Concord MA, USA) as a "graphics body" (Figure 4A).

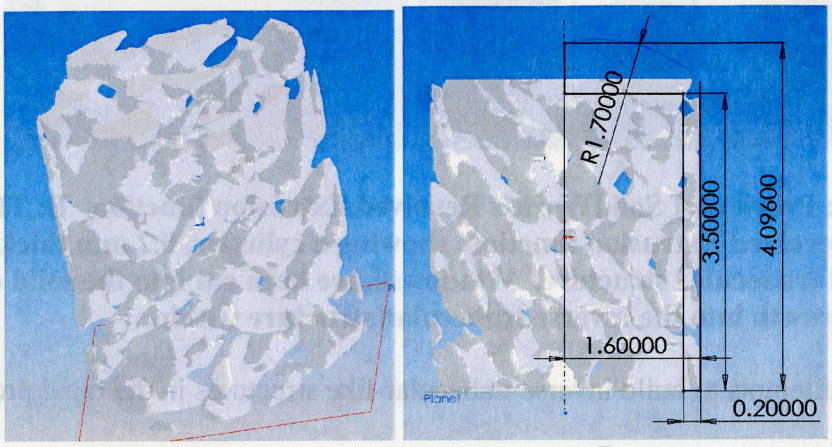

A B

Figure 4 – A: View of imported STL file in SolidWorks. B: 2D sketch drawn onto the imported STL file. All dimensions shown are in millimeters.

Due to the large STL file size produced from CT scans, attempting to import an STL file as a solid body caused the SolidWorks program to crash. Therefore, it was necessary to open the STL file as a graphics body file, a file that could be seen but not directly manipulated.

Using the program's drawing tools, an outer cylindrical structure (or "jacket") was created by first drawing a 2D sketch (Figure 4B), which was revolved 360° around the central axis of the STL graphics body to create a cylindrical tube that was topped with a flat, rounded dome (Figures 5A and 5B).

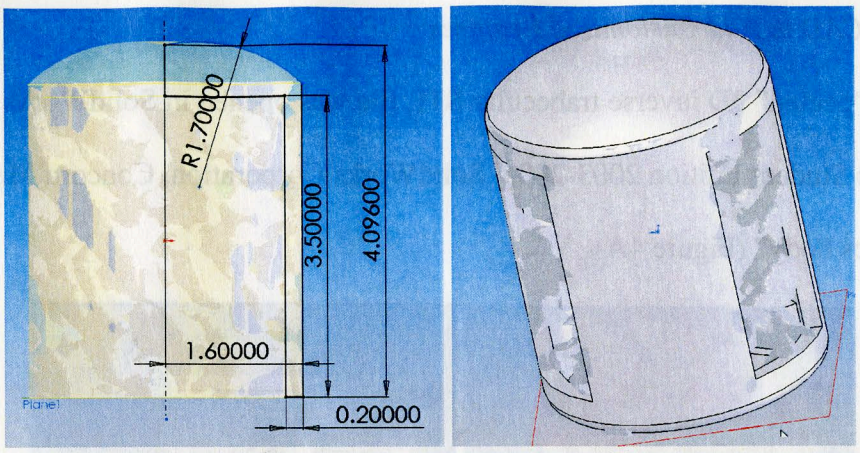

A B

Figure 5 – A: Preview of SolidWork's Revolved Extrusion function. B: The completed Revolved Extrusion function, showing a cylinder, 0.2 mm thick, around the imported trabecular structure. Windows have been cut into the solid cylinder to allow bone growth into the inverse trabecular structure within.

Prior attempts to build inverse trabecular-like structures in the rapid prototyping modeler revealed the need for a solid base for the structure to be built on. Another 2D sketch was drawn onto the bottom surface of the STL graphics body, resembling the spokes of a wheel (Figure 6A). The "Extruded Boss" function was used to merge the stabilization base to the outer cylindrical jacket. The finished solid stabilization base (Figure 6B) had openings wide enough to allow bone in-growth from the bottom of the scaffold, while serving as a solid foundation for the interior inverse trabecular pore structure.

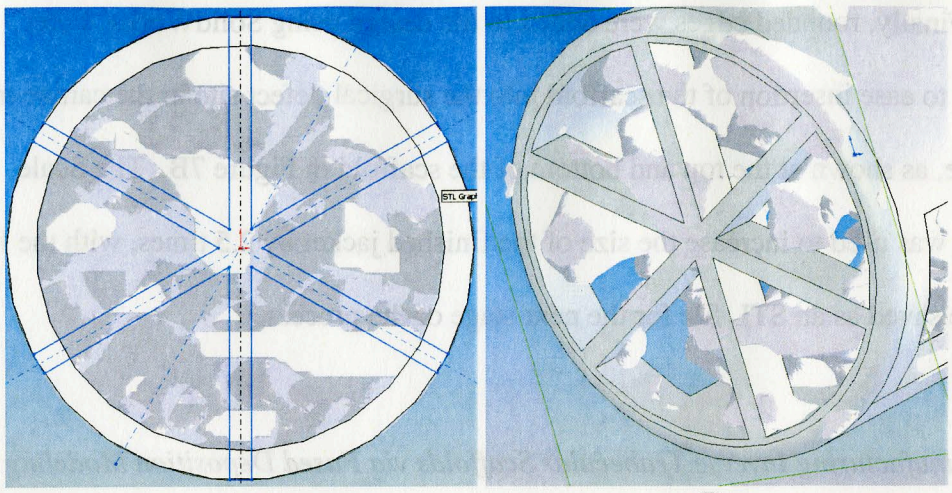

A B

Figure 6 – A: 2D sketch drawn onto the bottom of the 3D model, which defines the solid base of the scaffold. B: The finished base merged into the outer cylinder.

The outer jacket was added to provide space for attachment of strain gauges for an upcoming stage of the study, but access to the interior pore structure would be needed for bone in-growth. A 2d sketch was created and the "Extruded Cut" function was used to cut three windows, spaced 120° apart, into the outer cylinder to allow in-growth into the trabecular-like structure within (Figures 7A and 7B).

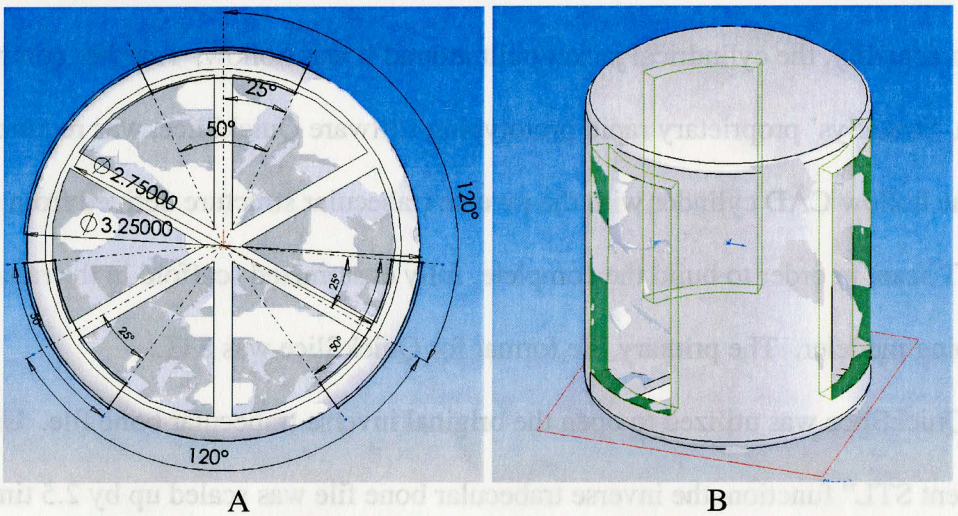

A B

Figure 7 – A: The 2D drawing of the windows to be cut out of the outer cylinder, spaced 120° apart, which provide access to the inner porosity. B: The finished structure with windows outlined in green.

Finally, rounded edges were added to the design using SolidWorks' Fillet function to ease insertion of the scaffold into the surgical defect site in the canine medial chondyle, as shown at the top and bottom of the scaffold in Figure 7B. The Scale function was used to increase the size of the finished jacket by 2.5 times, with the final structure saved as an STL file for the next stage of the process.

2.2.4 Manufacturing Inverse Trabecular Scaffolds via Fused Deposition Modeling

As in Experiment I, the inverse trabecular scaffolds were made out of PBT (Valox 315, GE Plastics, North America) using the same fused deposition modeler. The greater complexity of the inverse trabecular scaffolds required additional steps in the processing of the STL files in the modeler's software package.

2.2.5 Merging of Solid Cylindrical Structure with Inverse Trabecular Structure

As stated earlier, the imported STL file was not seen by SolidWorks as a solid body. In actuality, the cylindrical jacket built around it was hollow. Another computer program, StrataSys' proprietary rapid prototyping software QuickSlice, was required to merge the hollow CAD cylinder with the inverse trabecular structure derived from the micro CT scan, in order to build the complete, fully customized scaffold in the rapid prototyping modeler. The primary file format for QuickSlice was STL.

QuickSlice was utilized to open the original inverse trabecular bone file. Using the "Orient STL" function, the inverse trabecular bone file was scaled up by 2.5 times before being divided into slices by the "Slice" function. The newly sliced model was saved as an SSL file (a proprietary Stratasys file format) then closed.

QuickSlice was then used to open the SolidWorks-created jacket file, which was then sectioned into slices without scaling up (it was scaled up within SolidWorks). While the SolidWorks model was still open, the inverse trabecular bone slices could be merged into one structure with the jacket by using the File→Open function to select the SSL file of the inverse trabecular bone. In the Options menu, under Curve Options, the default "Remove Existing Curves" option was deselected, while the "Align from Bottom" and "Merge Intersecting Curves" options were selected. After closing the Options menu, and clicking OK in the Open File window, the two separate structures were shown to have merged into one object comprised of a series of slices.

2.2.6 Setting QuickSlice Parameters

Once the two sets of SSL files had been merged, raster parameters could be set to build the complete object in the rapid prototyping modeler. The raster parameters determine how the area of each slice or layer was filled in. For the inverse trabecular scaffolds, the porosity of the structure was obtained from the CT scan, so raster parameters were selected such that the solid portions of the structure were filled in with PBT.

Under the "Options" tab in the QuickSlice main screen, inches were chosen as the default working units. After clicking on the "Roads" tab, all of the slices (visualized as a stack of red lines) were highlighted by drawing a box around them using the mouse pointer. After clicking on "New Set," then "Advanced," the raster parameters were chosen for the manufacturing of the inverse trabecular scaffolds (Table 2).

Table 2: Raster Parameters for the Inverse Trabecular Scaffold group.

Parameters	Values
Air-gap Between Perimeter & Fills (in)	-0.003
Air-gap Between Raster Fills (in)	-0.003
Road Width of Perimeter (in)	0.0155
Road Width of Raster Fills (in)	0.0155
Raster Angles (degrees)	0, -90

Through trial and error, it was found that changing the speed at which the extrusion tip moved across each scaffold layer while depositing material changed the quality of the finished scaffold. If the speed was set too high, the PBT was not extruded so much as pulled in fine strands across each scaffold layer, leaving a fragile, overly porous structure that would easily crumble. If the speed was set to low, the PBT would not be deposited as filaments, but as irregularly-shaped blobs. As a result, the finished scaffold lacked porosity. To set the tip speed, the mouse pointer was moved over the "Materials" box at the top of the "Set Detail Values" window. By right-clicking anywhere in that white box, and choosing "Override," the "Override Material-Dependent Values" window was opened. The speed values for the perimeter and raster were decreased from the default 800 to 500. The units associated with these numbers were not stated.

After closing the "Override Material-Dependent Values" and "Set Detail Values" windows, and clicking the Ok button, the supports tab was chosen. Under the "Supports" tab, the "Create Base" button was clicked, accepting the default values for "Oversize" and "Levels." This placed a layer of support material (P-400 Release, Stratasys, Inc., Eden Prairie MN, USA) down as a barrier between the foam base on which the scaffolds were built and the scaffold itself. Upon returning to the "Roads" tab, the "Create Roads" button was clicked, which created the paths the extrusion assembly of the modeler would

take to fill in each layer of the scaffold. The completed file was then exported as a StrataSys Machine Language (SML) file for building in the modeler.

Within the modeler, the extrusion temperatures used for the model material (PBT) and the support material (P-400 Release) were 255^{O}C and 265^{O}C, respectively. A total of 24 inverse trabecular scaffolds were produced in the modeler. These were divided into four subgroups (n = 6 each). Group 0 scaffolds were kept dry before being placed in the CT scanner then mechanically compressed. Group 1 scaffolds were soaked for one month in 0.09% saline at 37^{o} before CT scanning and mechanical testing. Groups 2 and 3 were soaked in 0.09% saline at 37^{o} for two months and three months respectively before tomographic scanning and mechanical testing.

2.2.7 Design and Manufacture of the Complex Pore Structure Scaffolds

Prior to the development of the inverse trabecular scaffolds, a cylindrical scaffold similar in design to that of the jacket was utilized in a canine model (48), as shown in Figures 3A, B, and C. The term "complex pore structure" refers to the honeycomb-like pore structure created by choosing appropriate raster parameters in QuickSlice, as was done in Experiment I. For Experiment II, a large group of these scaffolds were manufactured for comparison to the inverse trabecular scaffolds. This comparison was carried out by evaluating the effect of in vitro degradation on mechanical properties and morphological features.

2.2.8 CAD Design of the Complex Pore Structure Scaffolds

As with the outer cylinder jacket created for the inverse trabecular scaffold, a 2D sketch was drawn in SolidWorks, then revolved 360° around an axis to produce a solid cylinder topped by a rounded dome. The "Extruded Cut" function was used to remove the upper segment of the dome, leaving a flat surface. The complete structure had a diameter of 8.9 mm and a height of 11.3 mm (Figure 8).

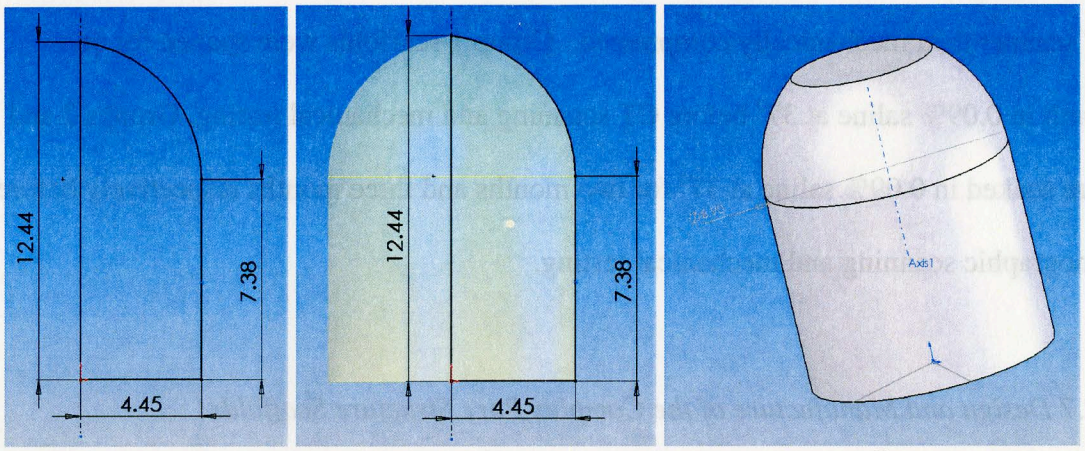

A B C

Figure 8 – A: 2D Sketch that will be revolved into a solid structure. B: The preview of the revolved sketch. C: the completed solid structure, with top section removed to create a flattened dome.

To allow bone ingrowth, a set of three vertically arranged holes (1 mm in diameter each) was placed in the outer structure of the cylinder using the 2d sketch tools and the extruded cut function. The circular pattern function was used to place three sets of these holes (spaced 120° apart) into the outer surface of the cylinder (Figure 9).

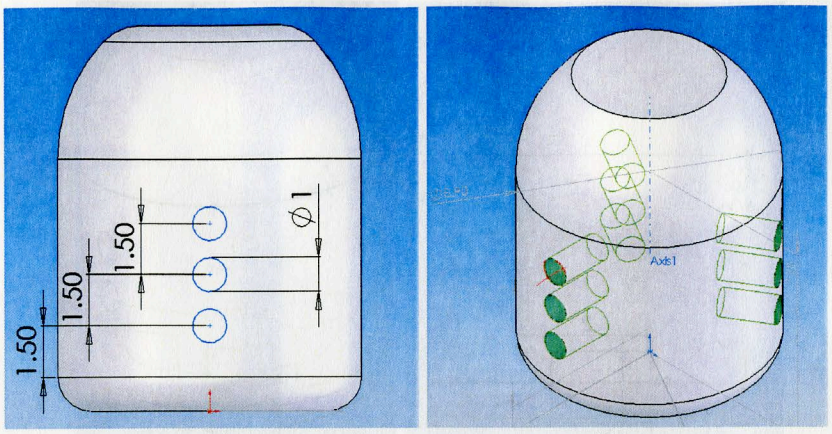

A B

Figure 9 – A: 2D sketch of one set of three vertically placed holes. The Extruded Cut function was used to cut those holes into the solid scaffold design, then the Pattern function copied those three holes two more times, separating them by 120,° as shown (outlined in green) in 9B. Figures 9A and 9B also show the rounded bottom edge, added for ease of surgical insertion, which was created using the Fillet function.

The scaffolds used in the study by Szivek et al (48) had three strain gauges, spaced 120° apart, attached to the outer surfaces. Space had to be made in the scaffolds to accomodate the wires leading from each strain gauge, so "2D Sketch" and the "Extruded Cut" function were used to make a 2 mm by 2 mm square hole (to a depth of 3 mm) through the outer surface of the scaffold along the bottom edge. The "Circular Pattern" function was again used to create a total of 3 holes, spaced 120° apart (Figure 10).

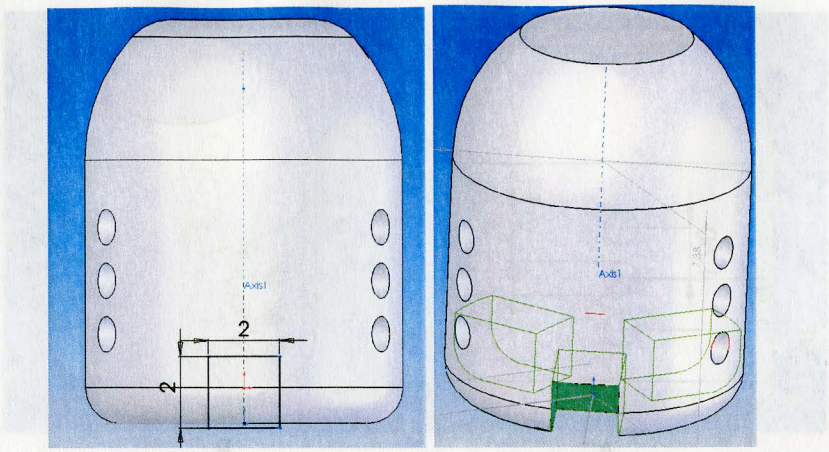

A B

Figure 10 – A: 2D sketch of the cutout drawn onto the base of the 3D scaffold model to accomodate the strain gauge wires. As in Figure 9B, Figure 10B shows three sets of such holes, spaced 120° apart, outlined in green.

To decrease the path length for bone in-growth (perpendicular to the longitudinal axis of the scaffold), a hole measuring 3.5 mm in diameter and 6.5 mm in depth was cut into the bottom of the scaffold using the "Extruded Cut" function. This left an open volume in the center of the scaffold (Figure 11).

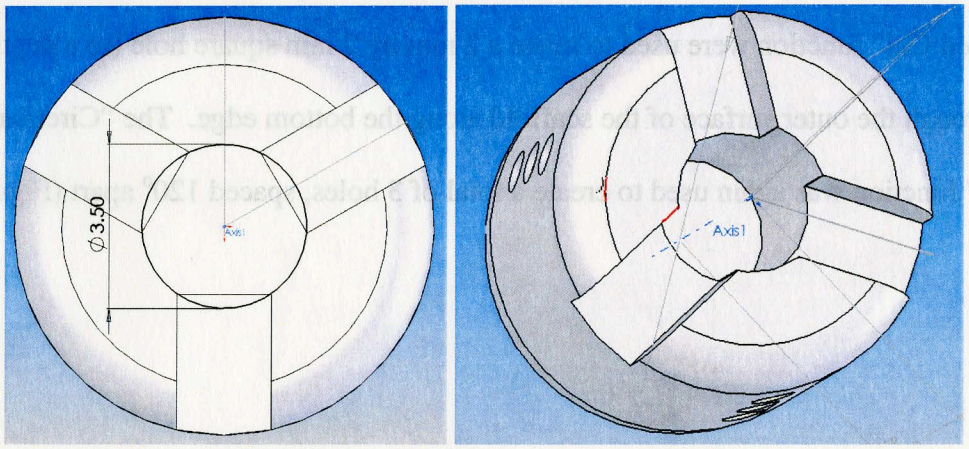

A B

Figure 11 – A: 2D sketch, defining the cylinder cutout in the center of the scaffold, drawn onto the bottom surface of the 3D structure. B: The hollow core following use of the Extruded Cut fuction.

The cutouts placed along the bottom of the scaffold to create space for strain gauge wires left three protruding structures that resembled the feet of a stool. After

manufacturing a previous scaffold design in the modeler, it was found that one or more of these feet could easily break off during surgery as the scaffold was being press-fit into place. A ring structure was added to stabilize these "feet" using the "Extruded Boss" function (Figure 12).

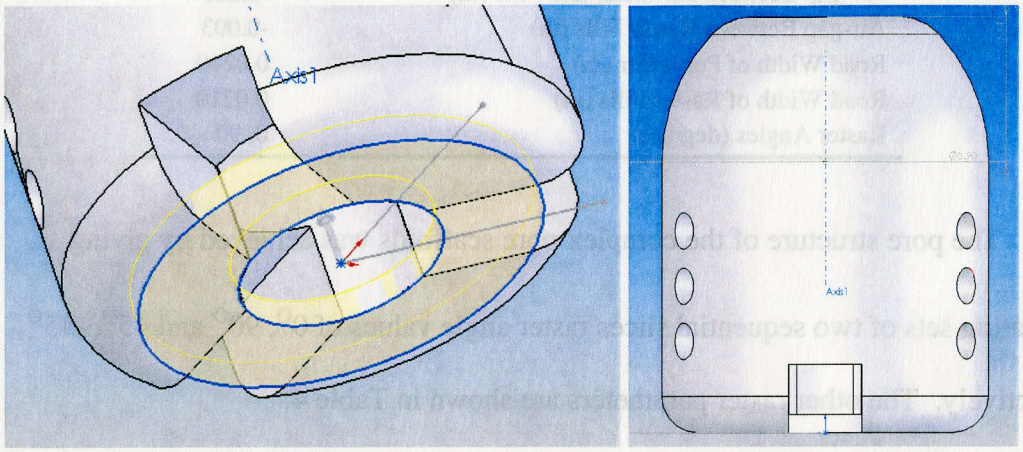

A B

Figure 12 – A: The Extruded Boss preview created from a 2D sketch of concentric circles drawn onto the bottom surface of the scaffold. B: The finished ring feature, merged into the bottom of the solid scaffold model. Strain gauge wires are threaded through the cutouts and out of the center hole.

Finally, as with the inverse trabecular scaffolds, the sharp edges of the design were rounded off using the fillet function to ease insertion of the complex pore structure scaffold into the surgically-created defect. The finished 3D model was then exported as an ASCII STL file.

2.2.9 QuickSlice Parameters for Complex Pore Structure Scaffolds

To mimic the subchondral layers of the canine medial chondyle, the dome portion of the complex trabecular scaffold was made solid by setting raster parameters so that the raster fills overlapped each other as each layer was built, leaving no open space between

them. The QuickSlice raster parameters for the slices that made up the solid dome are shown in Table 3:

Table 3: Raster Parameters used to make the solid dome of the Complex Pore Structure Scaffolds.

Parameters	Values
Air-gap Between Perimeter and Fills (in)	-0.003
Air-gap Between Raster Fills (in)	-0.003
Road Width of Perimeter (in)	0.0210
Road Width of Raster Fills (in)	0.0210
Raster Angles (degrees)	0, 90

The pore structure of the complex pore scaffolds was achieved by giving alternating sets of two sequential slices raster angle values of 0^{o}, 90^{o} and 45^{o}, -45^{o} respectively. The other raster parameters are shown in Table 4.

Table 4: Raster parameters used to make the porous portion of the Complex Pore Structure Scaffolds.

Parameters	Values
Air-gap Between Perimeter and Fills (in)	-0.003
Air-gap Between Raster Fills (in)	0.030
Road Width of Perimeter (in)	0.0210
Road Width of Raster Fills (in)	0.0210
Raster Angles (degrees)	0, 90, 45, -45

In Experiment II, the same FDM processing conditions were used as those listed in section 2.1.2, and the manufactured complex pore structure scaffolds were divided into subgroups as described in section 2.2.6.

2.2.10 In Vitro Degradation of Scaffolds

For each scaffold group besides Group 0 Inverse Trabecular and Group 0 Complex Pore Structure, six scaffolds each were placed in a total of six 50 ml centrifuge tubes (Catalogue No. 21008-178, VWR International, West Chester, PA USA). 30 ml of

0.09% saline solution was poured onto each scaffold and the tubes were sealed with a cap. The tubes were agitated enough to cause the scaffolds to sink to the bottom, and then were placed in an incubator set at 37°C. Every three days, the saline solution was exchanged for fresh solution. At the end of the designated time period, the scaffolds were removed from the saline-filled centrifuge tubes and drained on a paper towel before being scanning in the micro CT, and mechanically compressed.

2.2.11 Morphological Analysis of the Inverse Trabecular and Complex Pore Structured Scaffolds using Micro CT

For each test group of each scaffold type (Group 1, Group 2, and Group 3) the six saline-soaked scaffolds were placed into the sample holder of the μCT and scanned at standard resolution (250 x-ray projections, 512 X 512 pixel bitmap images, with resolution of 18 μm), with an integration time of 160 ms. The scaffolds were scanned three at time using the batch scanning function of the scanner.

On the scanned image of the scaffold, an outline was drawn around the outer edge of the scaffold with the free-hand drawing tool. This outline was copied onto successive slices until a VOI was created encompassing the entire scaffold. A Sigma-Gauss of 1.2, a support of 2, and a threshold of 50 were input into the scanner's segmentation program. Using the software accompanying the micro CT scanner, the morphological properties of porosity, connectivity density, trabecular spacing, trabecular number, and trabecular thickness were obtained to measure the effect of the saline treatment on scaffold structure.

2.2.12 Mechanical Testing of the Inverse Trabecular and Complex Pore Structured Scaffolds

Following micro CT scanning, all 24 test scaffolds (six scaffolds in each of the eight subgroups) were prepared for mechanical testing as previously discussed in section 2.1.4.

Each test scaffold was compressed axially on a mechanical test system (Model 810, MTS, Minneapolis, MN, USA) using a 200 kg load cell at a displacement rate of 4.2 mm/min, until failure. There was no preconditioning or preload on any of the scaffolds. For each compression test, load (kgf) and stroke (mm) were collected simultaneously with data collection software (LabView 5.0.1, National Instruments, Austin, TX) through a Ni-DAQ data acquisition board into a Macintosh G4 computer and saved into a spreadsheet. Ultimate compressive stress (defined as the stress at which the first failure of the scaffold occurs) and apparent modulus, the slope of each scaffold's linear stress-strain curve, was calculated for each scaffold.

2.2.13 Statistical Analysis

Statistical analysis was performed using a Kruskal-Wallis test because kurtosis was noted in some of the measured parameters. Apparent modulus, ultimate compressive stress, porosity, connectivity density, trabecular number, thickness, and spacing were the dependant variables while scaffold type and time were the independant variables used for the statistical analysis. A p value of less than 0.05 was considered statistically significant.

3 Results:

3.1 Experiment I

3.1.1 Morphological Analysis Using Micro CT Scanning

Average porosity values for the five scaffold groups ranged from 62.11 ± 0.36% for the trabecular 2p54trab group to 79.58 ± 0.35% for the group that had the largest simple linear pores, 90deg50 (Figure 13). There was no significant difference ($p < 0.05$) between the porosity of the trabecular bone sample from which the 2p54trab group was created (57.92 ± 0.04%) and the trabecular scaffolds (62.11 ± 0.36%). The two scaffold types whose rasters were laid 1.27 mm apart, 90deg50 and 9045deg50 had the highest porosity values.

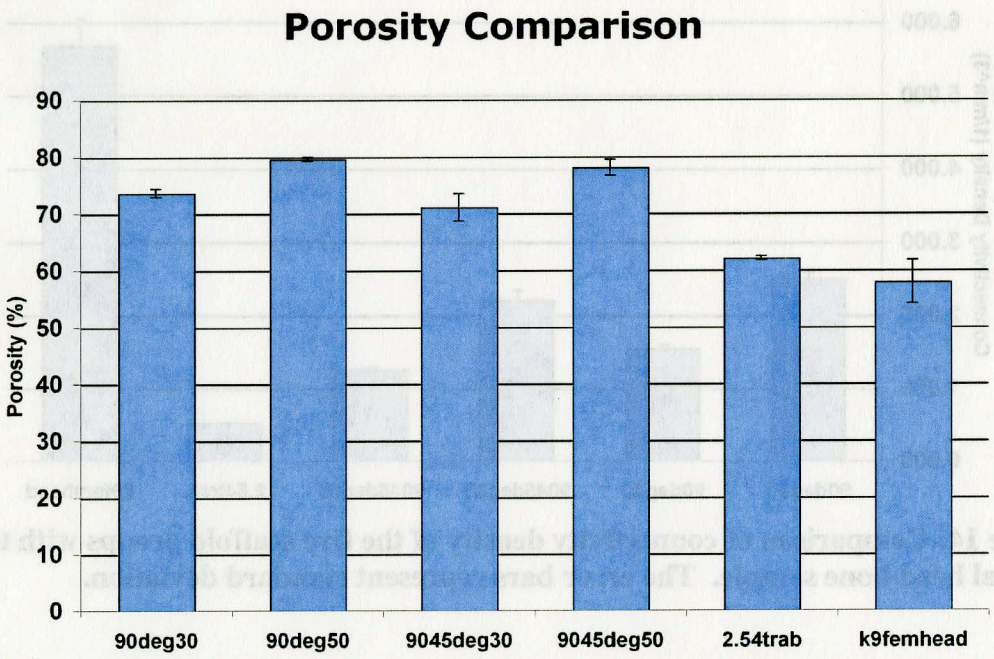

Figure 13: Scaffold group porosity comparison. "k9femhead" denotes the femoral head trabecular bone sample. The error bars represent standard deviation. For each scaffold group, n =6, while n = 4 for the k9femhead group.

In comparison to the connectivity density value of 5.68 ± 0.37 mm^{-3} for the trabecular bone sample, the connectivity density values of the five scaffold groups ranged

from 0.521 ± 0.013 mm^{-3} for the 2p54trab group to 2.505 ± 0.084 mm^{-3} for the simple linear pore scaffold group 90deg30 (Figure 14).

The trabecular separation value of the bone sample was 0.43 ± 0.03 mm. The average spacing for the five experimental scaffold groups ranged from 0.628 ± 0.032 mm for the complex interconnected pore group 9045deg30 to 1.132 ± 0.009 mm for the simple linear pore scaffold group 90deg50 (Figure 15). The average trabecular spacing value of the trabecular 2p54trab group was 1.085 ± 0.009 mm, approximately 2.3 times greater than that of the original bone sample.

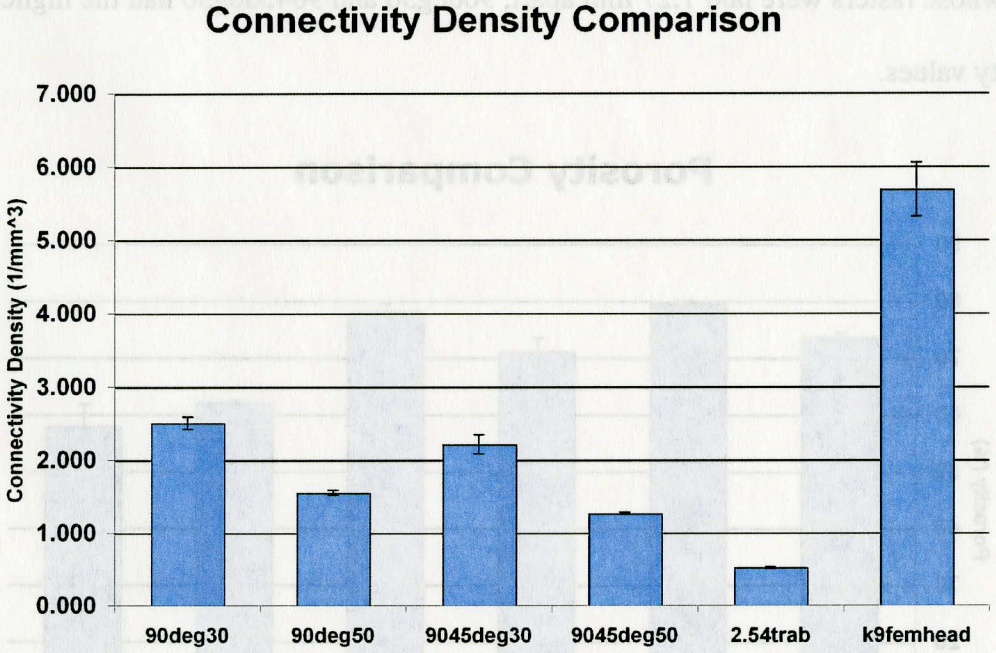

Figure 14: Comparison of connectivity density of the five scaffold groups with the femoral head bone sample. The error bars represent standard deviation.

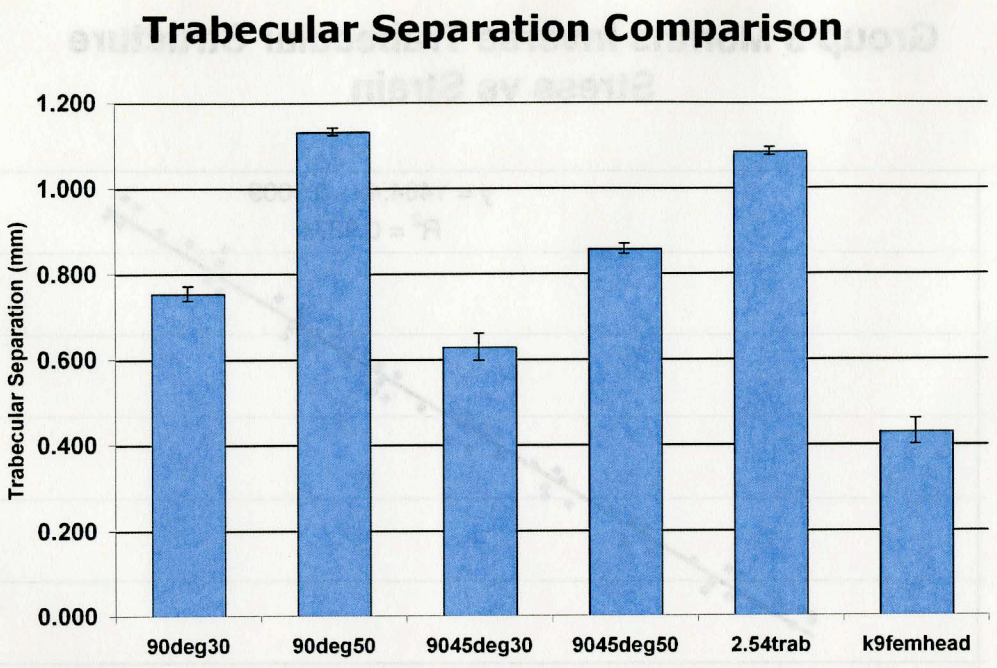

Figure 15: Comparison of trabecular separation among the five scaffold groups and the femoral head bone sample. The error bars represent standard deviation.

3.1.2 Mechanical Testing Results

3.1.2.1 Dry Scaffolds

A representative stress-strain curve is shown in Figure 16. When compressed at 49 N/s, the stiffness of the scaffold groups ranged from 2.46 ± 0.55 MPa for the complex interconnected pore structured 9045deg50 group to 5.11 ± 1.89 MPa for the simple linear pore structured of the 90deg30 scaffold group (Figure 17). For both the simple and complex scaffold groups, compressive stiffness decreased as pore size increased. The 2p54trab group had a compressive stiffness of 4.94 ± 1.19 MPa, which was most similar to that of the simple linear pore group 90deg30 and significantly stiffer ($p < 0.05$) than either of the scaffold groups with complex pore structures.

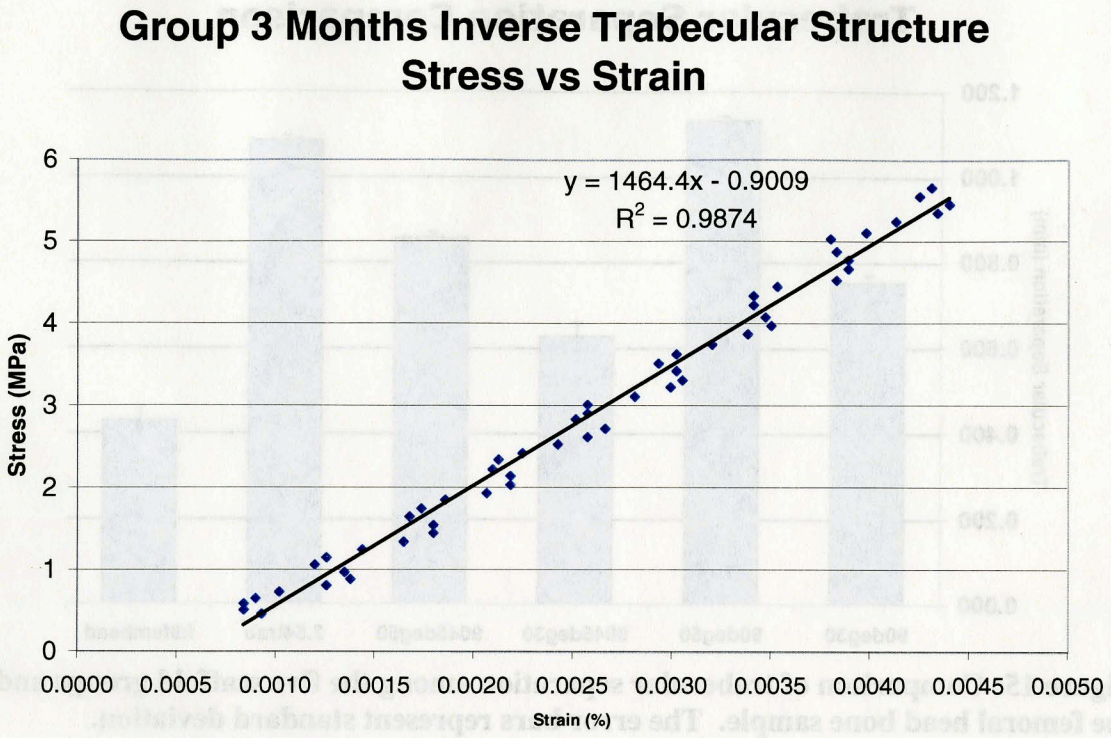

Figure 16: A representative scaffold stress vs. strain curve. The linear portion of the curve has been isolated and is shown here.

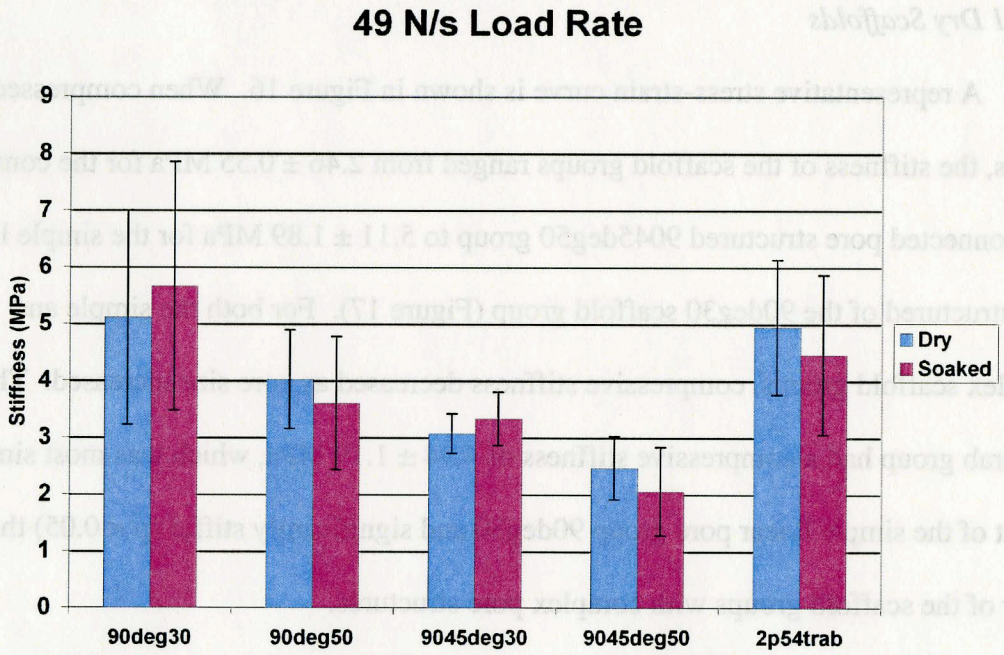

Figure 17: Scaffold stiffness at the 49 N/s compression load rate.

For the dry scaffolds compressed at 294 N/s, the compressive stiffness values nearly doubled for most scaffold groups and ranged from 3.86 ± 1.08 MPa for the complex interconnected pore structured 9045deg50 group to 10.44 ± 2.09 MPa for the simple linear pore 90deg30 group (Figure 18). The trabecular scaffold group had the second highest compressive stiffness value at 9.43 ± 0.93 MPa.

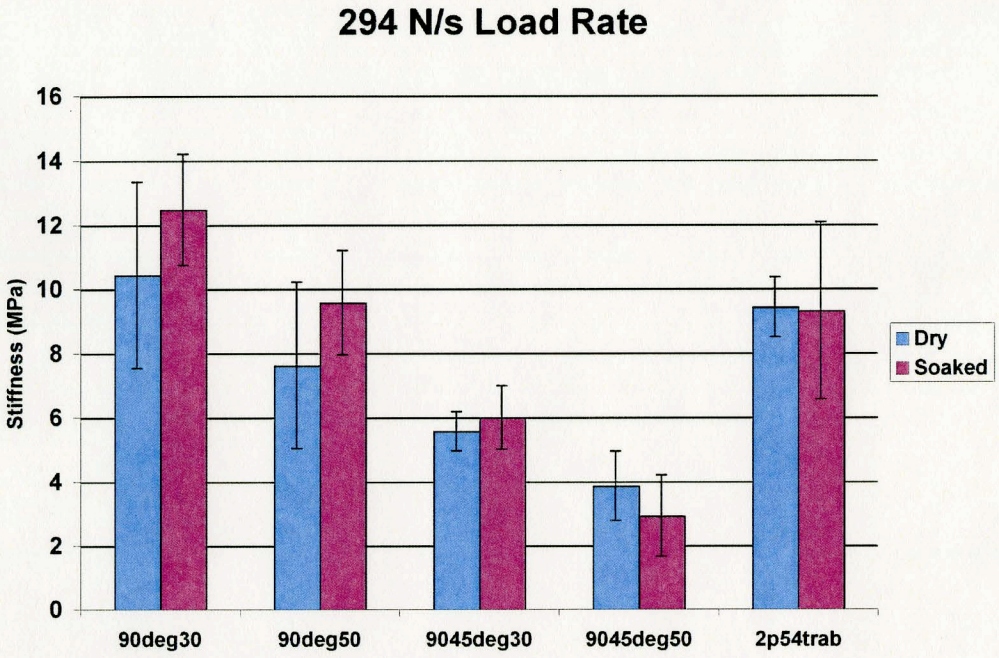

Figure 18: Scaffold stiffness at the 294 N/s load rate.

3.1.2.2 Soaked Scaffolds

At the 49 N/s load rate, the compressive stiffness for scaffolds soaked in 0.09% NaCl solution for 7 days ranged from 2.05 ± 0.77 MPa for the 9045deg50 complex interconnected pore scaffold group to 5.66 ± 2.19 MPa for the simple linear pore 90deg30 scaffold group. The 2p54trab group had the second highest compressive stiffness value at 4.46 MPa ± 1.4 MPa (Figure 17).

For most soaked scaffold groups, the compressive stiffness values roughly

doubled at the 294 N/s compression rate (Figure 18). They ranged from 2.93 ± 1.27 MPa for the complex interconnected pore structured 9045deg50 group to 12.47 ± 1.73 MPa for the simple linear pore structured 90deg30 group, with the 2p54trab group having the third highest compressive stiffness value of 9.32 ± 2.76 MPa.

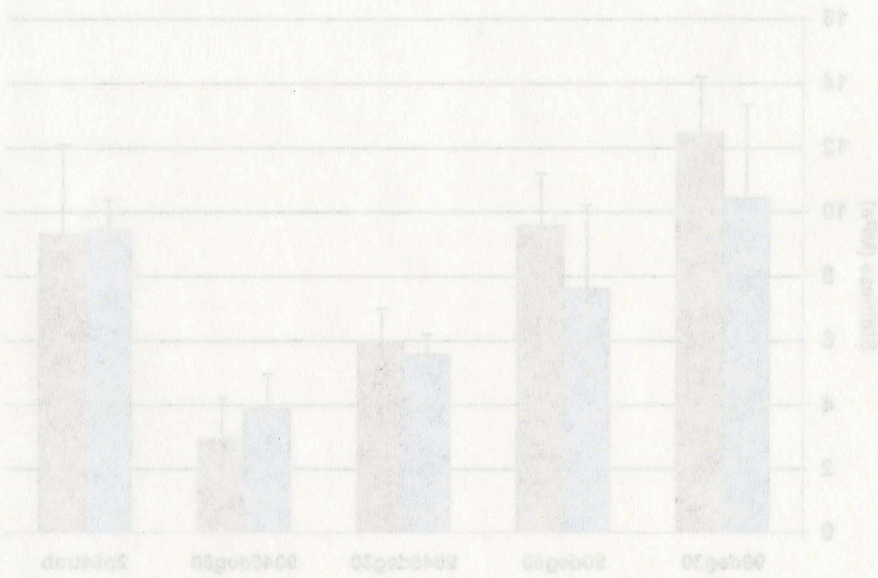

3.2 Experiment II

3.2.1 Micro CT Analysis of Structural Changes Due to Degradation

Using the μCT scanner's accompanying morphological analysis software, porosity, connectivity density, trabecular number, trabecular thickness, and trabecular spacing were measured for each scaffold type at several time points. This was done to assess structural change following soaking in saline at 37°C.

3.2.1.1 Porosity

The scanner software program does not report porosity. It reports instead a ratio of bone volume to total volume (BV/TV). The total volume is that which is defined as the VOI created during the segmentation process, while the "bone" volume refers to the pixels of each slice within the VOI whose brightness matches or exceeds the chosen threshold value for the material comprising the sample. In this case, the sample material is not bone, but PBT, requiring a lower threshold value than would be typically used for bone (i.e. 275). The threshold value chosen for the PBT scaffolds was 50. For this experiment, the porosity of each scaffold was defined as 1- (BV/TV).

The porosity values for the Inverse Trabecular and Complex Pore Structure scaffolds for each month are shown in Table 5:

Table 5: Porosity values for dry and soaked scaffolds.

Scaffold Type	Month 0 (% ± SD)	Month 1 (% ± SD)	Month 2 (% ± SD)	Month 3 (% ± SD)
Inverse Trabecular	48.57 ± 0.84	51.31 ± 0.20	49.47 ± 1.95	50.57 ± 1.67
Complex Pore	48.67 ± 2.33	48.35 ± 1.77	48.53 ± 0.91	49.19 ± 0.60

There was no significant change in porosity for either scaffold type throughout the test period, as well as no significant difference in porosity between the two scaffold types at

any time point (Figure 19).

3.2.1.2 Connectivity Density

Throughout the test period, there was virtually no change, for either scaffold type, in connectivity density (Table 6, Figure 20), which is the measure of the average number of connections that must be broken to separate a porous object into two parts (50). There was however, a significant difference between the scaffold types, with the Complex Pore scaffolds having an average connectivity density 5.78 times greater than that of the Inverse Trabecular scaffolds.

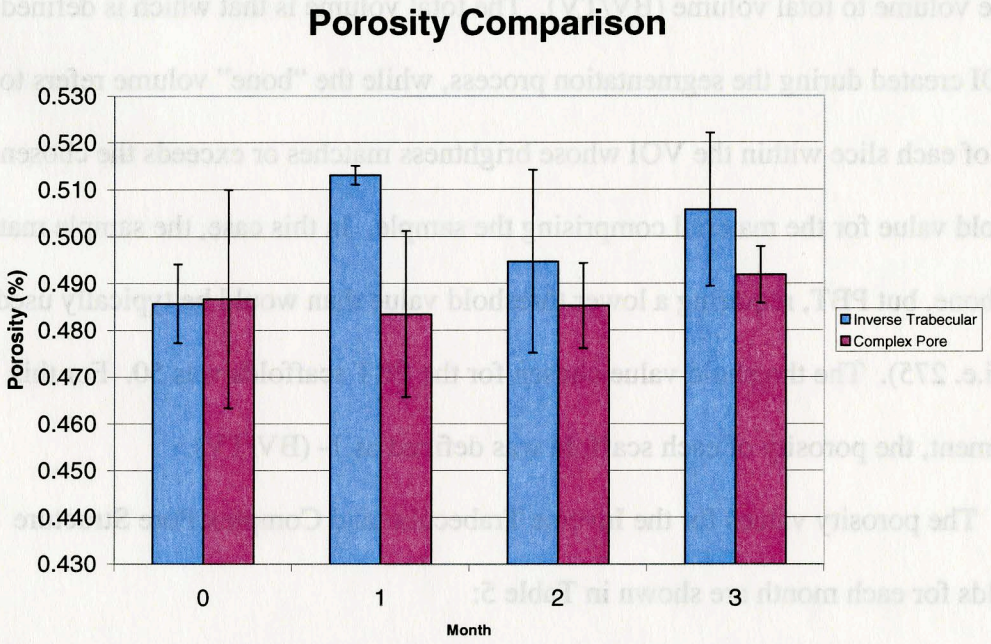

Figure 19: Porosity comparison between Inverse Trabecular and Complex Pore scaffold types, showing a significant difference between the average porosity of each scaffold type, but no significant change in either scaffold type with regard to time.

Table 6: Connectivity density for dry and soaked scaffolds.

	Month 0—dry (mm^{-3} ± SD)	Month 1 (mm^{-3} ± SD)	Month 2 (mm^{-3} ± SD)	Month 3 (mm^{-3} ± SD)
Inverse Trabecular	0.520 ± 0.008	0.449 ± 0.095	0.484 ± 0.079	0.542 ± 0.026
Complex Pore	2.770 ± 0.548	3.041 ± 0.974	2.790 ± 0.245	2.859 ± 0.234

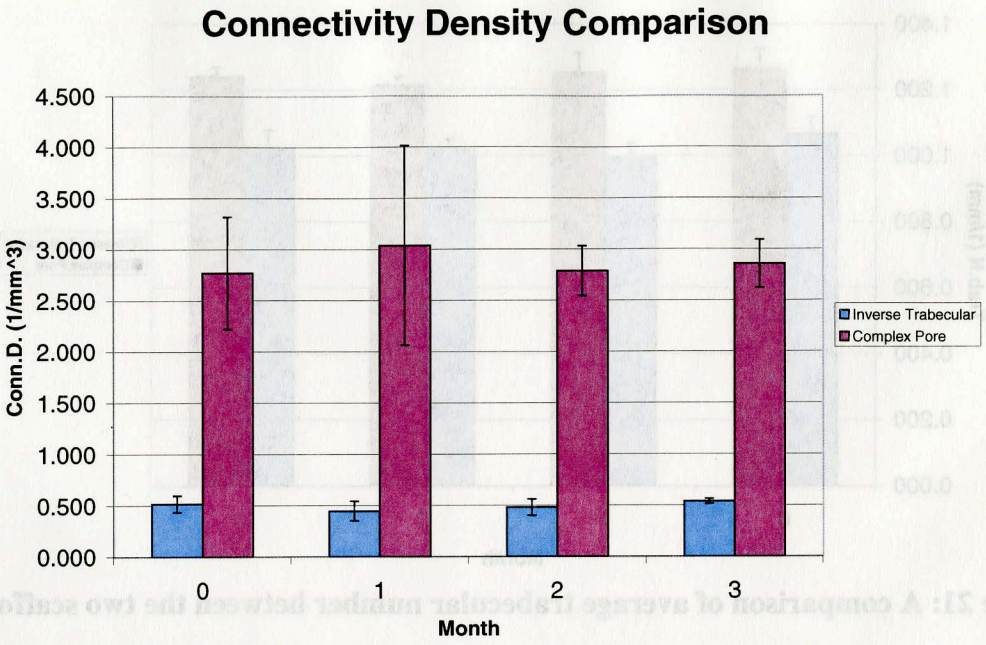

Figure 20: Average connectivity density values for each scaffold type. A large difference in connectivity density values can be seen between scaffold types, but no significant difference in values from month to month for either scaffold type.

3.2.1.3 Trabecular Number

As seen with connectivity density and porosity, there was virtually no change in the number of trabecular connections per millimeter within the porous scaffolds through month 3 (Table 7). There was a difference in the average trabecular number value between the two scaffold types. The Complex Pore scaffolds had average trabecular number values 21.2% greater than the Inverse Trabecular Scaffolds (Figure 21).

Table 7: Trabecular Number per mm for dry and soaked scaffolds.

	Month 0—dry (mm^{-1} ± SD)	Month 1 (mm^{-1} ± SD)	Month 2 (mm^{-1} ± SD)	Month 3 (mm^{-1} ± SD)
Inverse Trabecular	1.066 ± 0.052	0.994 ± 0.046	1.020 ± 0.029	1.024 ± 0.055
Complex Pore	1.264 ± 0.062	1.253 ± 0.061	1.213 ± 0.026	1.240 ± 0.030

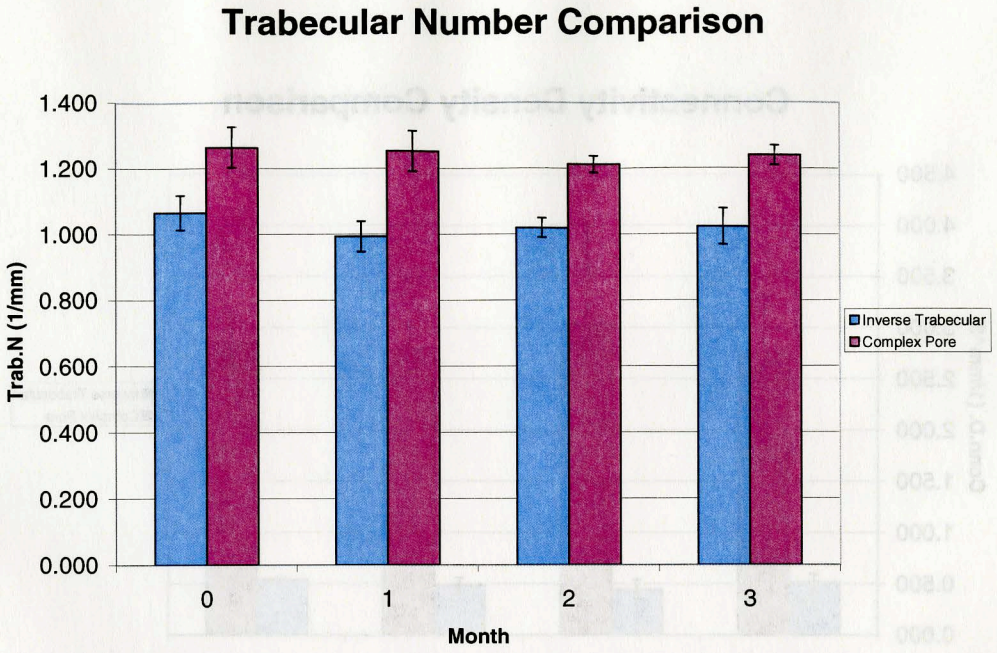

Figure 21: A comparison of average trabecular number between the two scaffold types.

3.2.1.4 Trabecular Thickness

The trabecular thickness values (Table 8) showed the greatest difference between scaffold types, second only to connectivity density. The average thickness of trabecular connections was an average of 46.7% greater among the Inverse Trabecular scaffolds than in the Complex Pore scaffold type (Figure 22). Despite the obvious difference between scaffold types, there was no significant difference in trabecular thickness between time-points.

Table 8: Trabecular Thickness in millimeters for dry and soaked scaffolds.

	Month 0—dry (mm ± SD)	Month 1 (mm ± SD)	Month 2 (mm ± SD)	Month 3 (mm ± SD)
Inverse Trabecular	0.722 ± 0.077	0.674 ± 0.045	0.707 ± 0.032	0.717 ± 0.076
Complex Pore	0.380 ± 0.035	0.382 ± 0.040	0.373 ± 0.008	0.368 ± 0.011

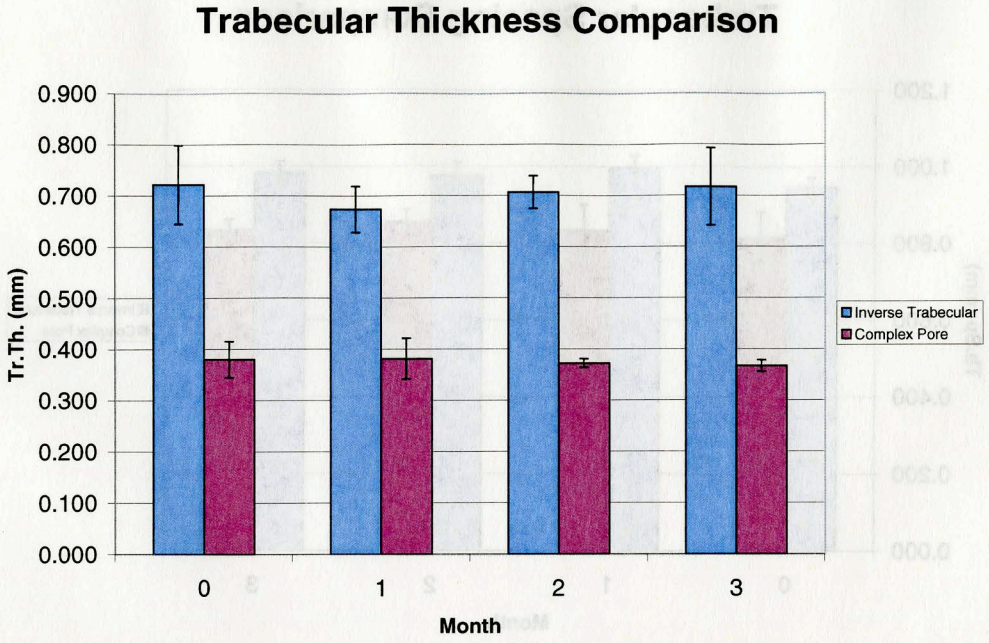

Figure 22: Trabecular thickness comparison between the Inverse Trabecular and Complex Pore Structure scaffold types. Again, there is a clear difference in average trabecular thickness values between the two types, but no significant change in trabecular thickness over time.

3.2.1.5 Trabecular Spacing

As with porosity, connectivity density, trabecular number, and trabecular thickness, the average distance between trabecular struts, or trabecular spacing, did not significantly change throughout the three month test period (Table 9). There was again a significant difference between scaffold types, with the average trabecular spacing of the Inverse Trabecular scaffolds being 17% greater than that of the Complex Pore scaffolds (Figure 23).

Table 9: Trabecular spacing in millimeters for dry and soaked scaffolds.

	Month 0—dry (mm ± SD)	Month 1 (mm ± SD)	Month 2 (mm ± SD)	Month 3 (mm ± SD)
Inverse Trabecular	0.946 ± 0.025	0.998 ± 0.031	0.976 ± 0.036	0.984 ± 0.030
Complex Pore	0.815 ± 0.069	0.834 ± 0.068	0.856 ± 0.033	0.833 ± 0.029

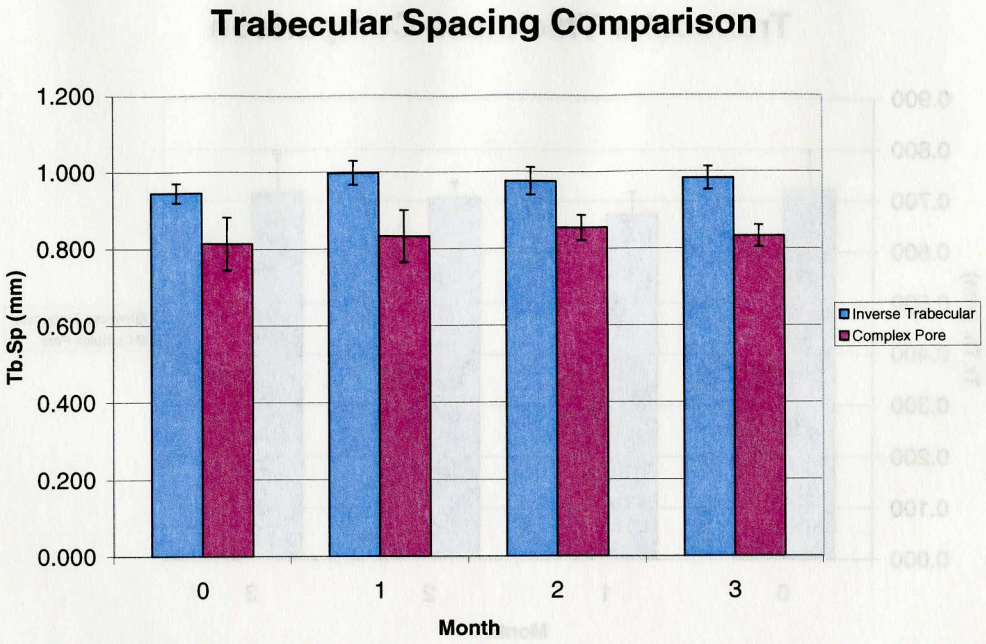

Figure 23: Average trabecular spacing values for the Inverse Trabecular and Complex Pore scaffold types.

3.2.2 Mechanical Testing Results

3.2.2.1 Ultimate Compressive Stress (UCS)

For the Inverse Trabecular scaffolds, the stress at which the first failure was recorded ranged from 3.96 ± 0.985 MPa to 5.01 ± 2.43 MPa. The UCS values for the Complex Pore scaffolds were nearly twice as great, ranging from 8.70 ± 1.81 MPa to 9.41 ± 2.27 MPa (Table 10). While there was a clear difference in UCS values between the scaffold groups, there was no significant change in ultimate compressive stress with regard to time (Figure 24).

Table 10: Ultimate compressive stress for dry and soaked scaffolds.

	Month 0 (MPa ± SD)	Month 1 (MPa ± SD)	Month 2 (MPa ± SD)	Month 3 (MPa ± SD)
Inverse Trabecular	4.48 ± 1.56	4.95 ± 0.88	5.01 ± 2.43	3.96 ± 0.99
Complex Pore	9.41 ± 2.27	9.01 ± 2.75	9.34 ± 1.87	8.70 ± 1.81

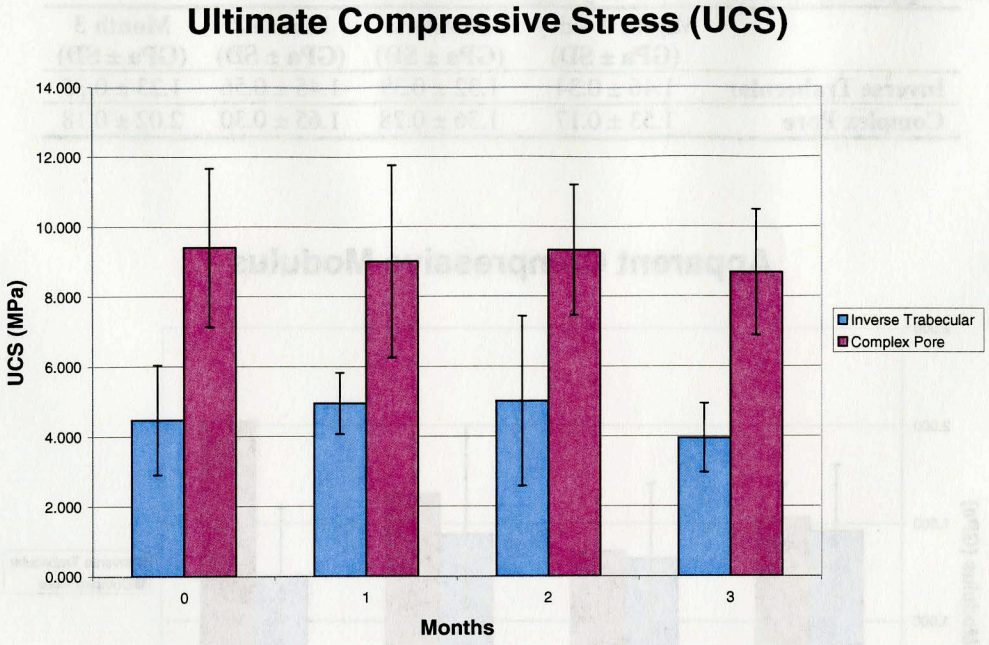

Figure 24: Average ultimate compressive stress values for the Inverse Trabecular and Complex Pore scaffolds. No significant change in UCS was seen with time for either scaffold type.

3.2.2.2 Apparent Compressive Modulus

For groups 0, 1, and 2, there was little difference in apparent modulus between the Inverse Trabecular scaffolds and the Complex Pore scaffolds (Figure 25). For month 3, there was some divergence between scaffold types that was statistically significant, though the p value (0.021) was still relatively high in comparison to the analysis of all other variables. A possible explanation for the increase in apparent compressive modulus after soaking in 37°C saline for 90 days is that two of the original six scaffolds in the Month 3 group were inadvertently lost. The smaller sample size may have skewed the mechanical testing results. The apparent modulus values for the Inverse Trabecular scaffolds ranged from 1.231 ± 0.349 GPa to 1.464 ± 0.335 GPa, and from 1.360 ± 0.281 GPa to 2.022 ± 0.176 GPa for the Complex Pore scaffolds (Table 11).

Table 11: Apparent modulus for dry and soaked scaffolds.

	Month 0 – dry (GPa ± SD)	Month 1 (GPa ± SD)	Month 2 (GPa ± SD)	Month 3 (GPa ± SD)
Inverse Trabecular	1.46 ± 0.34	1.32 ± 0.39	1.45 ± 0.56	1.23 ± 0.35
Complex Pore	1.53 ± 0.17	1.36 ± 0.28	1.65 ± 0.30	2.02 ± 0.18

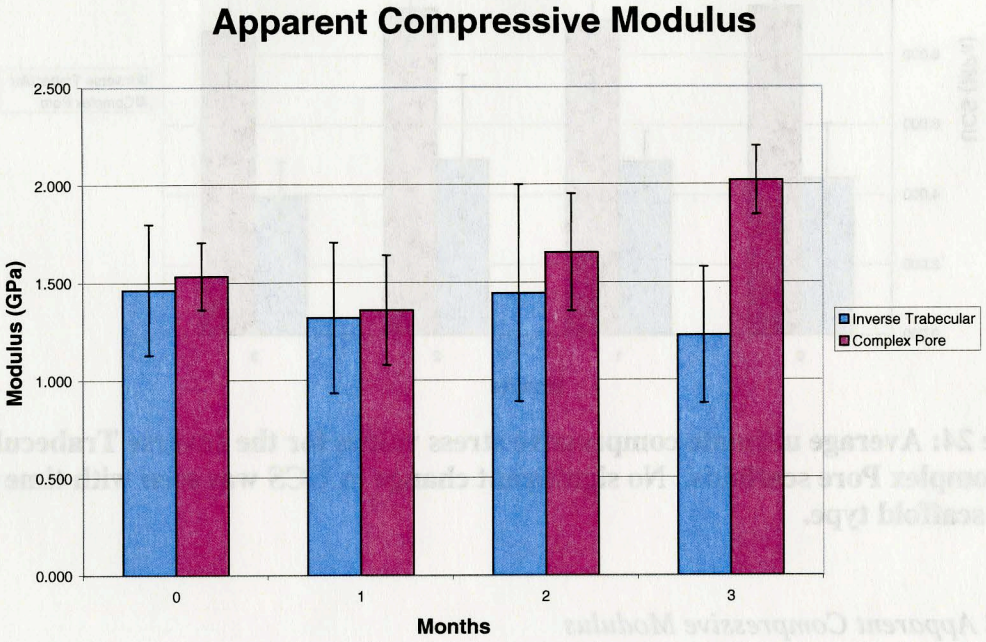

Figure 25: A comparison of the average apparent modulus of the Inverse Trabecular and Complex Pore scaffolds. While the values for months 0, 1, and 2 showed essentially no difference between in apparent modulus between the two scaffold types, by month 3, a significant difference (p = 0.02) between the two appeared.

4 Discussion

4.1 Experiment I

The purpose of this study was to develop and test a manufacturing process that combined high resolution imaging technology and freeform fabrication to replicate the unique tissue microstructure of trabecular bone with a resorbable polymer.

4.1.1 Morphometric comparison

The quality of trabecular bone can be characterized by its mechanical properties, chemical composition, and microarchitecture (51). When endeavoring to create a biomimetic bone scaffold, a synthetic duplication of the chemical composition of bone is not yet possible. However, utilizing high resolution imaging technologies, free-form fabrication techniques, and a polymer or ceramic formulation with appropriate mechanical properties it is possible to closely simulate the mechanical properties and microarchitecture of trabecular bone.

The volume fraction (and porosity) of human cadaveric bone samples from the femoral neck have been reported as 0.29 ± 0.05 (porosity 71% ± 5%) by Bayraktar, et al (52) and 0.16 ± 0.07 (porosity 84% ± 7%) by Kabel, et al (53). Bayraktar, et al (2004) calculated the volume fraction for their samples using the Archimedes principle, while Kabel, et al (1997) used a 3D morphometric program. Porosity values for trabecular bone were also reported (54) using cylindrical transiliac crest trabecular bone samples obtained from 70 patients (32 women, 38 men, with a mean age 68 ± 16 years). These samples underwent 3D morphometric analysis via μCT, and then were sectioned for 2D histomorphometric analysis to allow comparison of the two techniques. The mean BV/TV ratio reported by Muller, et al (54) was 14.48 ± 5.34% for the μCT-analyzed

samples, corresponding to a mean porosity of 85.5 ± 5.34%. These published porosity values (52-54) are on the same order as the porosities of the five scaffold types produced for this study. The mean porosity of the trabecular scaffold group was less than that of human cadaveric samples reported in the literature, but nearly identical to that of the porous canine femoral neck sample from which it was produced.

In a study assessing the impact of the connectivity density of cancellous bone on its elastic properties (53) fifty-five trabecular specimens from six anatomical regions (calcaneous, proximal tibia, distal and proximal femur, proximal humerus, and lumbar vertebral bodies) were collected and microtomed to a slice thickness of 20 μm to 25 μm. Digital photos of the slices were reconstructed into a 3D voxel model for micro finite element analysis and morphological analysis. The connectivity density for this series was reported as 3.36 ± 1.50 mm^{-3} and the volume fraction for these specimens was 0.16 ± 0.07 with a corresponding porosity of 84 ± 7%. Though the 2p54trab scaffold group was created from a μCT scan of a canine trabecular bone sample, it was the four scaffold groups with designed pore structures whose connectivity density values fell within the range of these published observations (53). The mean connectivity density value for the trabecular-like scaffold group (0.521 ± 0.013 mm^{-3}) was lower. This may have been the result of the resolution limitations of the fused deposition modeler used in this study because the modeler was originally designed to build larger models. The 3D scaffold CAD model was scaled up 2.54 times to gain better resolution, but it is apparent that the process must be further refined or that a modeler with better resolution must be utilized to achieve scaffold connectivity densities that better match natural bone.

Muller, et al (54) reported mean separation values for the μCT-evaluated samples of 0.77 ± 0.35 mm, which are on the same order as those of the scaffolds in the trabecular scaffold group in this study. However, the mean calculated trabecular spacing was significantly less than that of the canine sample from which the 3D CAD model was created (0.47 mm). This may also be due to the aforementioned modeler resolution issue.

4.1.2 The Use of Fused Deposition Modeling

Fused deposition modeling has been used to produce tissue engineering scaffolds with designed, interconnected pore structures like the simple and complex porous scaffolds produced for this study for both in vitro and in vivo studies. Several investigators (5, 49, 55, 56) have used fused deposition modeling to produce porous polymer scaffolds with interconnected pore structures. In this study, FDM was utilized to produce scaffolds made of polybutylene terephthalate (PBT), a semi-crystalline polyester that has been used in copolymer formulations in other biomedical applications (49) and which can be readily formed into a suitable filament for the modeler used. Hutmacher, et al, (5) Cao, et al, (55) and Darling and Sun, (56) used fused deposition modeling to produce polycaprolactone (PCL) scaffolds. Hutmacher, et al (2001) reported porosity values, measured by an ultrapycnometer, as 55% and 56% for their two complex scaffold designs. However, using porosimetry, scaffold porosity was measured as 61 ± 1% for both scaffold designs (5). That was nearly identical to the porosity measured for the trabecular scaffolds produced in this study. Hutmacher, et al (2001) also performed mechanical testing of the polycaprolactone scaffolds, reporting a compressive stiffness of 41.9 ± 3.5 MPa for dry scaffolds with a honeycomb-like raster angle pattern of

0°/60°/120° and 29.4 ± 4.0 MPa for the same scaffolds that had been soaked in a phosphate-buffered saline solution at 37°C for 1 day prior to compression testing (5). The scaffolds produced with a more complex pore structure (raster angle pattern 0°/72°/144°/36°/108°) had a lower dry compressive stiffness of 20.2 ± 1.7 MPa. The compressive stiffness value for the saline-soaked scaffolds was essentially unchanged when compared with unsoaked scaffolds at 21.5 ± 2.9 MPa (5). Like the more complex structured scaffolds produced by Hutmacher, et al (2001), the 9045deg30 and 9045deg50 scaffold groups in our study also had significantly lower stiffness values than their simpler counterparts. Overall, the dry compressive stiffness values for the polycaprolactone scaffolds were substantially higher than the values observed for the PBT scaffolds tested in Experiment I. However, unlike the PCL scaffolds, soaking the scaffolds in saline at 25°C for seven days did not cause a change in stiffness for the five PBT scaffold groups. PBT is known to have low water absorption, making it less susceptible to hydrolysis than polymers such as polycaprolactone.

Darling and Sun (56) produced porous polycaprolactone scaffolds via FDM and used micro computed tomography to analyze multiple structures produced with two different extrusion tip sizes, 10 mils (0.254 mm) and 7 mils (0.178 mm). 2D analysis of CT slices was performed to assess strut width and pore width of the samples. Pore width, which is analogous to trabecular separation, for the 10 mil samples ranged from 196 ± 56 μm (0.196 ± 0.056 mm) to 292 ± 40 μm (0.292 ± 0.040 mm) and from 120 ± 62.8 μm (0.120 ± 0.0628 mm) to 772 ± 33.5 μm (0.772 ± 0.0335 mm) for the 7 mil samples (56). The trabecular separation measurements reported in the present study were generally higher than the pore width values reported by Darling and Sun (56). This could be due to

the fact that a 12 mil extrusion tip was used along with a larger raster gap width setting. Darling and Sun did not report raster gap width settings for their scaffold designs.

4.1.3 Use of Micro CT to produce Bone Tissue Engineering Scaffolds

An alternative rapid prototyping technique was used in conjunction with micro CT to produce biomimetic trabecular bone scaffolds by Peng, et al (57). 3D gel lamination, a process similar to 3D printing, was used to translate 3D data sets created from micro CT scans of canine femoral head samples into biphasic calcium phosphate ceramic scaffolds. The authors claim that morphometric analysis revealed no significant difference ($p < 0.05$) between the trabecular bone samples and trabecular scaffold samples with respect to BV/TV (porosity), trabecular thickness (Tb.Th), trabecular number (Tb.N), or trabecular bone pattern factor (Tb.Pf) (57). Tb.Th, Tb.N, and Tb.Pf, were not assessed in Experiment I, but the reported 62% porosity (57) was nearly identical to that of the polymer trabecular scaffolds produced for the present study. The biphasic calcium phosphate scaffolds likely had a more similar radio-opacity to trabecular bone, enabling use of more similar micro CT threshold values between the bone samples and scaffold samples. This may have aided comparison of morphometric features between their structures. The ceramic material accounted for the large disparity in average compressive stiffness values reported by Peng, et al (57) (0.464 ± 0.036 GPa) and those of the trabecular bone scaffolds reported in Experiment I, which were also significantly lower than the compressive stiffness of trabecular bone. Trabecular bone compressive stiffness values have been reported by Martens et al as 0.616 ± 0.707 GPa, 0.174 ± 0.084 GPa, and 0.063 ± 0.007 GPa (58) for femoral neck samples compressed

along the x, y, and z axes respectively and as 18.0 ± 2.8 GPa by Bayraktar et al (2004). The gap between the compressive stiffness values reported by Martens et al and Bayraktar et al is characteristic of the wide range of elastic moduli values of human trabecular bone samples, as reported in many other studies (52, 58).

4.2 Experiment II

4.2.1 Biomimetic Approach to Bone Tissue Engineering Scaffold Design

One of the chief advantages of combining high resolution imaging, CAD, and free-form fabrication techniques to produce tissue engineering constructs is the potential to create a more patient-specific scaffold whose microstructure can be made to resemble that of the native tissue being repaired (4, 59, 60). This is especially important given that cell function is closely related to the way in which the cells are organized in space to form a three-dimensional tissue (61, 62). Because of the importance of scaffold microstructure in tissue engineering, a number of researchers are following a biomimetic approach to scaffold design by using computer aided manufacturing or other techniques to copy natural structures such as trabecular bone.

Quadrani et al (2005) scanned a human trabecular femoral head bone sample (donor was a male, age 50) in a micro CT scanner whose 30 μm resolution was on par with the scanner used in this experiment (61). The 3D data set produced from this scan was used to drive a stereolithography system to create trabecular bone-like specimens from a resin that was 17-28% cyclohexyldimethanol diglycidyl ether, 40-60% cycloaliphatic epoxy resin, and 2-8% photoinitiator. Morphological analysis consisted of measuring the pore size distribution on the acrylic scaffolds by sectioning them with a microtome and imaging each slice with a digital camera (61).

The CT-data derived acrylic constructs (whose material was stated to be inappropriate for bone tissue engineering) had a mean pore diameter of 0.569 ± 0.147 mm. The pore diameter can be considered analogous to the average distance between trabecular struts, or trabecular spacing, which for the Inverse Trabecular scaffolds produced for the present study ranged from 0.946 ± 0.025 mm to 0.984 ± 0.030 mm, nearly twice as great as that reported by Quadrani et al (61). It must be remembered that the scaffolds produced for the present study were created using an *inverse* trabecular structure, one purposely "eroded" to increase porosity. There was no mention of the degree to which the mean pore diameter of the acrylic scaffolds matched that of the human bone sample.

Unlike Quadrani et al (2005), Holy et al (2003) did not use an image based approach or rapid prototyping process to create scaffolds designed for bone tissue engineering. Their scaffolds were created via a novel combination of polymer precipitation and glucose crystal leaching that left a solid porous matrix made of poly(lactide-co-glycolide) (PLGA) whose structure was reported to be similar in appearance to trabecular bone (62).

The PLGA scaffolds became tissue engineering constructs (TECs) when seeded with bone-marrow-derived cells from rabbit iliac crests, cultured for 14 days, then implanted into 1.2 cm defects created in New Zealand White rabbit femurs. The TECs were held in place by titanium plates and screws (62).

Morphological analysis of the PLGA scaffolds was performed using scanning electron microscopy (SEM), mercury porosimetry, radiographs of the rabbits' femurs at t=0, 2, 4, 6, and 8 weeks postoperatively, and post-sacrifice histology (62).

The porosity of the PLGA scaffolds Holy et al produced ranged between 89% (measured by mercury porosimetry) and 92% (via image analysis) (62), and was approximately twice as great as that measured via micro CT analysis for the Inverse Trabecular scaffolds (48.6 ± 0.84 % to 50.6 ± 1.67%) and Complex Pore scaffolds (48.4 ± 1.77% to 49.2 ± 0.60%). The average pore diameter of the PLGA scaffolds was 1.44 ± 0.30 mm (62), about 50% greater than the trabecular spacing values reported for the Inverse Trabecular scaffolds (0.946 ± 0.025 mm to 0.998 ± 0.031 mm) and the Complex Pore scaffolds (0.815 ± 0.069 mm to 0.856 ± 0.033 mm).

Though the authors expected that the biodegradable PLGA scaffolds would be replaced by bone (62), there was no reported assessment of the degree of degradation of the scaffolds either in vitro or in vivo. Mechanical testing was not performed on the PLGA scaffolds, although the authors had ascertained in a previous study that their scaffolds possessed mechanical properties sufficient for cell colonization and matrix formation (63). The degree to which the implanted TECs would be capable of independent load bearing is unclear, because they were supported by titanium plates and screws. In one recent scaffold degradation study, Oh et al (2006), employing porous PLGA scaffolds created by salt crystal leaching, reported that scaffold modulus had dropped by half after two weeks in vitro degradation in 37°C phosphate buffered saline (pH 7.4), with a faster degradation rate during subcutaneous implantation in rats (64). Neither PBT scaffold type produced for this study showed a significant decrease in mechanical stiffness in up to three months immersion in 37°C saline, suggesting better long term load-bearing capabilities without the need for additional implants that must later be removed once the bone has healed.

While Holy et al (50, 62) state a biomimetic strategy was utilized, this does not appear to refer to the creation of the scaffolds themselves, but to the use of bone-marrow-derived cells seeded onto scaffolds whose microstructure serendipitously resembles trabecular bone. The reported process used to create the TECs could not, by itself, create patient-specific constructs designed to fill an irregular defect site. It would have to be combined with a molding or cutting process of some kind to create scaffolds having both the macro- and microstructure necessary to repair complicated defects.

The work of Van Cleynenbreugel et al (2002) focuses on creating scaffolds capable of filling irregular bone defects produced by the removal of benign bone tumors (65). In following a biomimetic approach, the authors are primarily concerned with matching the mechanical properties of their scaffolds to that of the surrounding normal tissue, so that mechanical loads within the scaffold are transferred to the cells seeded within, stimulating them to develop into bone tissue (65).

Clinical computed tomography (not micro CT) was performed, as part of a surgeon's pre-surgical planning, to obtain a 3D model of the tumor to be removed. By inverting the 3D volume of the defect, a model of the void to be filled by the scaffold can be obtained in a process similar to one employed by Hollister et al (2000) to fill craniofacial defects (66). The internal pore structure of the scaffold is created by Boolean subtraction of a 3D porous structure from the outer contour of the inverse defect.

Van Cleynenbreugel et al (2002), unlike Hollister et al (2000), did not utilize a rapid prototyping process to produce actual scaffolds, but performed finite element analysis (FEA) on the 3D scaffold model to estimate its mechanical properties and compare them to FEA of a 3D model of trabecular bone.

One of the current strategies for filling the voids left after tumor removal is to fill the defect with polymethyl methacrylate (PMMA) bone cement, a non-degradable material (67). For their 3D scaffold model analysis, Van Cleynenbreugel et al (2002) input the known elastic modulus value for PMMA, 3 GPa, into their FEA program, and calculated an apparent scaffold stiffness of 197 MPa, far lower than the apparent stiffness they calculated for trabecular bone (elastic modulus = 10 GPa), which was 847 MPa (65). Via iteration, the authors ultimately determined that their scaffold model called for a material whose elastic modulus was about 12.5 GPa (65). This elastic modulus would enable their scaffold model to have an apparent stiffness approximating that of trabecular bone, but is an elastic modulus much higher than that of biodegradable materials currently used in tissue engineering applications. Van Cleynenbreugel et al (2002) did not state a value for the compression rate chosen for their FEA. The compressive modulus of PBT is 2.5 GPa (68), and the Inverse Trabecular scaffolds produced for the present study had a apparent modulus that ranged from 1.23 ± 0.349 GPa to 1.464 ± 0.335 GPa, which were measured at a displacement rate of 4.2 mm/min. In this study, each compression trial was performed under displacement control; however, the calculated load rates for each scaffold type was 503.56 ± 143.14 N/sec for the Inverse Trabecular scaffolds, and 646.82 ± 124.05 N/sec for the Complex Pore scaffolds. The Complex Pore scaffolds' apparent modulus ranged from 1.36 ± 0.281 GPa to 2.02 ± 0.176 GPa. The apparent modulus values for each scaffold type fits within the range of elastic modulus values reported for human trabecular bone (69).

4.2.2 Scaffold Degradation Studies

While it is important to attempt to match the microstructure of the tissue being engineered, it is also necessary to understand how a tissue scaffold may withstand the in vivo environment. This is most often assessed using in vitro and in vivo degradation experiments.

Lin et al (2005) used a type of rapid prototyping, solid freeform fabrication (SFF) to produce wax molds for scaffolds whose pore structure had been designed to provide optimal distribution of material in order to display maximal stiffness under applied load (70). This design technique is known as topology optimization (71). The porous scaffolds were comprised of a composite of β-tricalcium phosphate incorporated into poly(propylene fumarate) (PPF/β-TCP), a material whose mechanical properties are said to increase during the early stages of degradation due to a cross-linking reinforcement mechanism (72-74). Though Lin et al (2005) were primarily interested in the bone forming capability of scaffolds seeded with cells transduced with an adenovirus to express Bone Morphogenic Protein 7 (BMP-7), 24 empty PPF/β-TCP scaffolds were also implanted subcutaneously in immuno-compromised mice (70). Within two weeks post-operatively, the apparent compressive modulus of the empty PPF/β-TCP scaffolds decreased by approximately 61.5%, from about 130 MPa (prior to implantation) to 55 MPA (after two weeks in vivo), and continued decreasing for the remainder of the twelve week experiment (70). The apparent compressive modulus of the transduced cell-seeded scaffolds also decreased dramatically within the first two weeks post-implantation, with the average value decreasing 53.8% from 130 MPa to 60 MPa. From week two to week twelve, the compressive modulus of the seeded scaffolds remained constant at

approximately 60 MPa, indicating that growing bone was compensating for the degrading composite (70). In comparison to the PPF/β-TCP scaffolds, the PBT scaffolds produced for the present study showed no significant decrease in apparent modulus over the course of three months.

This is in keeping with the results reported by Sakkers et al (1998), who produced mechanical test specimens (via injection molding) made of polyethylene oxide-polybutylene terephthalate (PEO-PBT) block co-polymers whose compositions ranged from 30% PEO - 70% PBT to 70% PEO - 30% PBT. The soft, amorphous PEO is strongly hydrophilic and rapidly degrading in comparison to the hard, semi-crystalline PBT (75).

The test specimens that had the highest compressive modulus were the ones made of 30% PEO – 70% PBT. Those that were initially tested dry had an average modulus of 274 ± 18.55 MPa, while those that had been tested wet (meaning they were kept in 37°C saline for five days prior to testing) had a slightly lower compressive modulus of 252 ± 15.56 MPa, indicating slight degradation of the PEO portion of the co-polymer. The same 30% PEO – 70% PBT scaffolds were implanted subcutaneously in goats for up to 25 weeks, and by three weeks in vivo, the compressive modulus decreased to 240 ± 3.67 MPa. At the nine week mark, the compressive modulus of the 30% PEO – 70% PBT specimens was essentially unchanged at 237 ± 33.82 MPa, and by 25 weeks in vivo, the compressive modulus was 237 ± 13.08 MPa. These results indicate that once the PEO degraded, the remaining PBT maintained its mechanical properties for over six months in vivo. While the apparent compressive modulus of the porous PBT scaffolds produced for this study fall at the low end of reported values for trabecular bone (69), making it less

likely that these scaffolds will cause stress-shielding that may lead to bone resorption (70), the slow degradation of PBT may limit the growth of regenerated tissue by degrading at a rate much slower than the growth rate of new bone. An "ideal" tissue engineering scaffold would degrade at a rate matching the growth rate of the tissue replacing it (5).

5 Conclusions

Fused deposition modeling shows promise as a versatile, solvent-free tissue-engineering scaffold manufacturing technique that requires virtually no post-processing. More work done to match the resolution of scaffold manufacturing processes to that of the imaging techniques that have made possible the creation of biomimetic structures would be valuable. However, this technique has already been shown to be capable of manufacturing scaffolds matching trabecular bone porosity. In combination with free form fabrication, micro computed tomography is useful for generating 3D scaffold structures for rapid prototyping, as well as morphological analysis of manufactured structures. The addition of computer aided drawing software packages allows the creation of fully customized and optimized tissue engineering constructs which open the door to additional applications to tissue regeneration.

6 Future Research

Future research in this area should include in vivo studies in which bone in-growth into Inverse Trabecular scaffolds is compared to bone growing into a more conventional porous polymer scaffold, as well as to normal bone, using typical bone quality parameters such as connectivity density and trabecular thickness. Such a study would allow assessment of the effect of a simulated natural microstructure on bone regeneration. In additional, use of bioactive agents such as bone morphogenic proteins (BMPs) and transforming growth factors (TGFs) deposited onto simulated natural microstructures can be seen as the next step towards truly biomimetic tissue engineering constructs.

7 References

1. "Who get's it?" [homepage on the Internet]. Available from: http://www.arthritis.org/conditions/diseasecenter/OA/oa_who.asp.

2. Seeherman HJ, Azari K, Bidic S, Rogers L, Li XJ, Hollinger JO, et al. rhBMP-2 delivered in a calcium phosphate cement accelerates bridging of critical-sized defects in rabbit radii. *J Bone Joint Surg Am.* 2006 Jul;88(7):1553-65.

3. Redman SN, Oldfield SF, Archer CW. Current strategies for articular cartilage repair. *Eur Cell Mater.* 2005 Apr 14;9:23,32; discussion 23-32.

4. Tsang VL, Bhatia SN. Three-dimensional tissue fabrication. *Adv Drug Deliv Rev.* 2004 Sep 22;56(11):1635-47.

5. Hutmacher DW, Schantz T, Zein I, Ng KW, Teoh SH, Tan KC. Mechanical properties and cell cultural response of polycaprolactone scaffolds designed and fabricated via fused deposition modeling. *J Biomed Mater Res.* 2001 May;55(2):203-16.

6. Karageorgiou V, Kaplan D. Porosity of 3D biomaterial scaffolds and osteogenesis. *Biomaterials.* 2005 Sep;26(27):5474-91.

7. Vacanti JP, Langer R, Upton J, Marler JJ. Transplantation of cells in matrices for tissue regeneration. *Adv Drug Deliv Rev.* 1998 Aug 3;33(1-2):165-82.

8. Athanasiou KA, Agrawal CM, Barber FA, Burkhart SS. Orthopaedic applications for PLA-PGA biodegradable polymers. *Arthroscopy.* 1998 Oct;14(7):726-37.

9. Yamaguchi M, Shinbo T, Kanamori T, Wang PC, Niwa M, Kawakami H, et al. Surface modification of poly(L: -lactic acid) affects initial cell attachment, cell morphology, and cell growth. *J Artif Organs.* 2004;7(4):187-93.

10. Cronin EM, Thurmond FA, Bassel-Duby R, Williams RS, Wright WE, Nelson KD, et al. Protein-coated poly(L-lactic acid) fibers provide a substrate for differentiation of human skeletal muscle cells. *J Biomed Mater Res A.* 2004 Jun 1;69(3):373-81.

11. Mann BK, West JL. Cell adhesion peptides alter smooth muscle cell adhesion, proliferation, migration, and matrix protein synthesis on modified surfaces and in polymer scaffolds. *J Biomed Mater Res.* 2002 Apr;60(1):86-93.

12. Berry CC, Campbell G, Spadiccino A, Robertson M, Curtis AS. The influence of microscale topography on fibroblast attachment and motility. *Biomaterials.* 2004 Nov;25(26):5781-8.

13. Tan J, Shen H, Saltzman WM. Micron-scale positioning of features influences the rate of polymorphonuclear leukocyte migration. *Biophys J.* 2001 Nov;81(5):2569-79.

14. Wan Y, Wang Y, Liu Z, Qu X, Han B, Bei J, et al. Adhesion and proliferation of OCT-1 osteoblast-like cells on micro- and nano-scale topography structured poly(L-lactide). *Biomaterials*. 2005 Jul;26(21):4453-9.

15. Srouji S, Maurice S, Livne E. Microscopy analysis of bone marrow-derived osteoprogenitor cells cultured on hydrogel 3-D scaffold. *Microsc Res Tech*. 2005 Feb;66(2-3):132-8.

16. Kim HJ, Kim UJ, Vunjak-Novakovic G, Min BH, Kaplan DL. Influence of macroporous protein scaffolds on bone tissue engineering from bone marrow stem cells. *Biomaterials*. 2005 Jul;26(21):4442-52.

17. Uematsu K, Hattori K, Ishimoto Y, Yamauchi J, Habata T, Takakura Y, et al. Cartilage regeneration using mesenchymal stem cells and a three-dimensional poly-lactic-glycolic acid (PLGA) scaffold. *Biomaterials*. 2005 Jul;26(20):4273-9.

18. Hutmacher DW. Scaffolds in tissue engineering bone and cartilage. *Biomaterials*. 2000 Dec;21(24):2529-43.

19. Orgill DP, Straus FH,2nd, Lee RC. The use of collagen-GAG membranes in reconstructive surgery. *Ann N Y Acad Sci*. 1999 Oct 30;888:233-48.

20. McGlohorn JB, Holder WD,Jr, Grimes LW, Thomas CB, Burg KJ. Evaluation of smooth muscle cell response using two types of porous polylactide scaffolds with differing pore topography. *Tissue Eng*. 2004 Mar-Apr;10(3-4):505-14.

21. Marei MK, Nouh SR, Saad MM, Ismail NS. Preservation and regeneration of alveolar bone by tissue-engineered implants. *Tissue Eng*. 2005 May-Jun;11(5-6):751-67.

22. Li H, Chang J. Preparation and characterization of bioactive and biodegradable wollastonite/poly(D,L-lactic acid) composite scaffolds. *J Mater Sci Mater Med*. 2004 Oct;15(10):1089-95.

23. Gomes ME, Sikavitsas VI, Behravesh E, Reis RL, Mikos AG. Effect of flow perfusion on the osteogenic differentiation of bone marrow stromal cells cultured on starch-based three-dimensional scaffolds. *J Biomed Mater Res A*. 2003 Oct 1;67(1):87-95.

24. Furuzono T, Kishida A, Tanaka J. Nano-scaled hydroxyapatite/polymer composite I. coating of sintered hydroxyapatite particles on poly(gamma-methacryloxypropyl trimethoxysilane)grafted silk fibroin fibers through chemical bonding. *J Mater Sci Mater Med*. 2004 Jan;15(1):19-23.

25. Gomes ME, Godinho JS, Tchalamov D, Cunha AM, Reis RL. Alternative tissue engineering scaffolds based on starch: Processing methodologies, morphology, degradation and mechanical properties. *Materials Science and Engineering: C*. 2002 May;20(1-2):19-26.

26. Li Z, Ramay HR, Hauch KD, Xiao D, Zhang M. Chitosan-alginate hybrid scaffolds for bone tissue engineering. *Biomaterials*. 2005 Jun;26(18):3919-28.

27. Li Z, Ramay HR, Hauch KD, Xiao D, Zhang M. Chitosan-alginate hybrid scaffolds for bone tissue engineering. *Biomaterials*. 2005 Jun;26(18):3919-28.

28. Mikos AG, Temenoff JS. Formation of highly porous biodegradable scaffolds for tissue engineering. *Electronic Journal of Biotechnology*. 2005 July;3(2)

29. Sherwood JK, Riley SL, Palazzolo R, Brown SC, Monkhouse DC, Coates M, et al. A three-dimensional osteochondral composite scaffold for articular cartilage repair. *Biomaterials*. 2002 Dec;23(24):4739-51.

30. McMains S. Layered manufacturing technologies. *Communications of the Association for Computing Machinery*. 2005;48(6):50-56.

31. Venuvinod PK, Ma W. Rapid prototyping: Laser-based and other technologies. Boston ; London: Kluwer Academic; 2004.

32. Cooper KG. Rapid prototyping technology: Selection and application. New York: Marcel Dekker; 2001.

33. Tan KH, Chua CK, Leong KF, Cheah CM, Gui WS, Tan WS, et al. Selective laser sintering of biocompatible polymers for applications in tissue engineering. *Biomed Mater Eng*. 2005;15(1-2):113-24.

34. Seitz H, Rieder W, Irsen S, Leukers B, Tille C. Three-dimensional printing of porous ceramic scaffolds for bone tissue engineering. *J Biomed Mater Res B Appl Biomater*. 2005 Aug;74(2):782-8.

35. Winder J, Bibb R. Medical rapid prototyping technologies: State of the art and current limitations for application in oral and maxillofacial surgery. *J Oral Maxillofac Surg*. 2005 Jul;63(7):1006-15.

36. Fisher JP, Holland TA, Dean D, Engel PS, Mikos AG. Synthesis and properties of photocross-linked poly(propylene fumarate) scaffolds. *J Biomater Sci Polym Ed*. 2001;12(6):673-87.

37. Matsuda T, Mizutani M. Liquid acrylate-endcapped biodegradable poly(epsilon-caprolactone-co-trimethylene carbonate). II. computer-aided stereolithographic microarchitectural surface photoconstructs. *J Biomed Mater Res*. 2002 Dec 5;62(3):395-403.

38. Maruo S, Ikuta K. Submicron stereolithography for the production of freely movable mechanisms by using single-photon polymerization. *Sensors and Actuators A: Physical*. 2002;100(1):70-76.

39. Lee G, Barlow JW. In: Selective laser sintering of bioceramic materials for implants. *Proceedings of solid freeform fabrication symposium*; August 9-11, 1993; Austin, TX USA. ; 1993.

40. Vail NK, Swain LD, Fox WC, Aufdlemorte TB, Lee G, Barlow JW. Materials for biomedical applications. Materials & Design. 1999/6/1;20(2-3):123-32.

41. Hutmacher DW. Scaffold design and fabrication technologies for engineering tissues--state of the art and future perspectives. *J Biomater Sci Polym Ed.* 2001;12(1):107-24.

42. Zein I, Hutmacher DW, Tan KC, Teoh SH. Fused deposition modeling of novel scaffold architectures for tissue engineering applications. *Biomaterials.* 2002 Feb;23(4):1169-85.

43. Sun W, Darling A, Starly B, Nam J. Computer-aided tissue engineering: Overview, scope and challenges. *Biotechnol Appl Biochem.* 2004 Feb;39(Pt 1):29-47.

44. Balshi SF, Wolfinger GJ, Balshi TJ. Surgical planning and prosthesis construction using computer technology and medical imaging for immediate loading of implants in the pterygomaxillary region. *Int J Periodontics Restorative Dent.* 2006 Jun;26(3):239-47.

45. Siebert H, Schleier P, Beinemann J, Fried W, Zenk W, Schumann D. Evaluation of individual ceramic implants made of bioverit with CAD/CAM technology to reconstruct multidimensional craniofacial defects of the human skull. *Mund Kiefer Gesichtschir.* 2006 May;10(3):185-91 (in German).

46. Schneider A, Kurtzman GM. Computerized milled solid implant abutments utilized at second stage surgery. *Gen Dent.* 2001 Jul-Aug;49(4):416-20.

47. Eufinger H, Pack M, Terheyden H, Wehmoller M. Experimental computer-assisted alloplastic sandwich augmentation of the atrophic mandible. *J Oral Maxillofac Surg.* 1999 Dec;57(12):1436,40; discussion 1440-1.

48. Szivek JA, Bliss CL, Geffre CP, Margolis DS, Deyoung DW, Ruth JT, et al. An instrumented scaffold can monitor loading in the knee joint. *J Biomed Mater Res B Appl Biomater.* 2006. DOI: 10.1002/jbm.b 30532

49. Szivek JA, Margolis DS, Garrison BK, Nelson E, Vaidyanathan RK, DeYoung DW. TGF-beta1-enhanced TCP-coated sensate scaffolds can detect bone bonding. *J Biomed Mater Res B Appl Biomater.* 2005 Apr;73(1):43-53.

50. DeHoff RT, Aigeltinger EH, Craig KR. Experimental determination of the topographical properties of three-dimensional microstructures. *Journal of Microscopy.* 1972:69-91.

51. Judex S, Boyd S, Qin YX, Miller L, Muller R, Rubin C. Combining high-resolution micro-computed tomography with material composition to define the quality of bone tissue. *Curr Osteoporos Rep.* 2003 Jun;1(1):11-9.

52. Bayraktar HH, Morgan EF, Niebur GL, Morris GE, Wong EK, Keaveny TM. Comparison of the elastic and yield properties of human femoral trabecular and cortical bone tissue. *J Biomech.* 2004 Jan;37(1):27-35.

53. Kabel J, Odgaard A, van Rietbergen B, Huiskes R. Connectivity and the elastic properties of cancellous bone. *Bone.* 1999 Feb;24(2):115-20.

54. Muller R, Van Campenhout H, Van Damme B, Van Der Perre G, Dequeker J, Hildebrand T, et al. Morphometric analysis of human bone biopsies: A quantitative structural comparison of histological sections and micro-computed tomography. *Bone.* 1998 Jul;23(1):59-66.

55. Cao T, Ho KH, Teoh SH. Scaffold design and in vitro study of osteochondral coculture in a three-dimensional porous polycaprolactone scaffold fabricated by fused deposition modeling. *Tissue Eng.* 2003;9 Suppl 1:S103-12.

56. Darling AL, Sun W. Free-form fabrication and micro-CT characterization of poly-epsilon-caprolactone tissue scaffolds. *IEEE Eng Med Biol Mag.* 2005 Jan-Feb;24(1):78-83.

57. Peng J, Wang AY, Sun MX, Xu WJ, Huang JX, Zhao B, et al. The preparation, structure evaluation and preliminary application of biomimetic biphasic calcium phosphate scaffold. *Zhonghua Wai Ke Za Zhi.* 2005 Jun 15;43(12):807-11 (in Chinese).

58. Martens M, Van Audekercke R, Delport P, De Meester P, Mulier JC. The mechanical characteristics of cancellous bone at the upper femoral region. *J Biomech.* 1983;16(12):971-83.

59. Leong KF, Cheah CM, Chua CK. Solid freeform fabrication of three-dimensional scaffolds for engineering replacement tissues and organs. *Biomaterials.* 2003 Jun;24(13):2363-78.

60. Hutmacher DW. Scaffold design and fabrication technologies for engineering tissues--state of the art and future perspectives. *J Biomater Sci Polym Ed.* 2001;12(1):107-24.

61. Quadrani P, Pasini A, Mattiolli-Belmonte M, Zannoni C, Tampieri A, Landi E, et al. High-resolution 3D scaffold model for engineered tissue fabrication using a rapid prototyping technique. *Med Biol Eng Comput.* 2005 Mar;43(2):196-9.

62. Holy CE, Fialkov JA, Davies JE, Shoichet MS. Use of a biomimetic strategy to engineer bone. *J Biomed Mater Res A.* 2003 Jun 15;65(4):447-53.

63. Holy CE, Shoichet MS, Davies JE. Engineering three-dimensional bone tissue in vitro using biodegradable scaffolds: Investigating initial cell-seeding density and culture period. *J Biomed Mater Res.* 2000 Sep 5;51(3):376-82.

64. Oh SH, Kang SG, Lee JH. Degradation behavior of hydrophilized PLGA scaffolds prepared by melt-molding particulate-leaching method: Comparison with control hydrophobic one. *J Mater Sci Mater Med.* 2006 Feb;17(2):131-7.

65. Van Cleynenbreugel T, Van Oosterwyck H, Vander Sloten J, Schrooten J. Trabecular bone scaffolding using a biomimetic approach. *J Mater Sci Mater Med.* 2002 Dec;13(12):1245-9.

66. Hollister SJ, Levy RA, Chu TM, Halloran JW, Feinberg SE. An image-based approach for designing and manufacturing craniofacial scaffolds. *Int J Oral Maxillofac Surg.* 2000 Feb;29(1):67-71.

67. Gitelis S, McDonald DJ. Surgery for bone and soft tissue tumors. Philadelphia, PA USA: Lippincott-Raven Publishers; 1998.

68. Kaplan WA (Ed). Resins and compounds. *Modern Plastics Encyclopedia 1999.* 1998;72(2):B187-B189.

69. Rho JY, Ashman RB, Turner CH. Young's modulus of trabecular and cortical bone material: Ultrasonic and microtensile measurements. *J Biomech.* 1993 Feb;26(2):111-9.

70. Lin CY, Schek RM, Mistry AS, Shi X, Mikos AG, Krebsbach PH, et al. Functional bone engineering using ex vivo gene therapy and topology-optimized, biodegradable polymer composite scaffolds. *Tissue Eng.* 2005 Sep-Oct;11(9-10):1589-98.

71. Lin CY, Lin C, Hollister SJ. In: A new approach for designing biodegradable bone tissue augmentation devices by using degradation topology optimization. *8th world multiconference on systemics, cybernetics, and informatics*; July 18-21, 2004; Orlando, FL USA. ; 2004.

72. Frazier DD, Lathi VK, Gerhart TN, Altobelli DE, Hayes WC. In: In vivo degradation of a poly(propylene-fumarate) biodegradable particulate composite bone cement. *Materials research society proceedings*; 1995.

73. Yaszemski MJ, Payne RG, Hayes WC, Langer R, Mikos AG. In vitro degradation of a poly(propylene fumarate)-based composite material. *Biomaterials.* 1996 Nov;17(22):2127-30.

74. Peter SJ, Miller ST, Zhu G, Yasko AW, Mikos AG. In vivo degradation of a poly(propylene fumarate)/beta-tricalcium phosphate injectable composite scaffold. *J Biomed Mater Res.* 1998 Jul;41(1):1-7.

75. Sakkers RJ, de Wijn JR, Dalmeyer RA, van Blitterswijk CA, Brand R. Evaluation of copolymers of polyethylene oxide and polybutylene terephthalate (polyactive): Mechanical behaviour. *J Mater Sci Mater Med.* 1998 Jul;9(7):375-9.

Appendix: Animal Subjects Approval

All procedures involving the use of animal tissue followed the Guidelines for the Care and Use of Laboratory Animals (Institute of Laboratory Animal Resources, 1996). This research was approved by The University of Arizona Institutional Animal Care and Use Committee (IACUC 05-003).